

Abstract

Measurement of total hadronic differential cross sections in the LArIAT experiment

Elena Gramellini

2018

6 Abstract goes here. Limit 750 words.

Measurement of total hadronic differential cross sections in the LArIAT experiment

A Dissertation
Presented to the Faculty of the Graduate School
of
Yale University
in Candidacy for the Degree of
Doctor of Philosophy

15 by
16 Elena Gramellini

¹⁷ Dissertation Director: Bonnie T. Fleming

18 Date you'll receive your degree

¹⁹

Copyright © 2017 by Elena Gramellini

²⁰

All rights reserved.

21

A mia mamma e mio babbo,

22

grazie per le radici e grazie per le ali.

23

To my mom and dad,

24

thank you for the roots and thank you for the wings.

²⁵ Contents

²⁶	Acknowledgements	vi
²⁷	0 Liquid Argon Detectors at the Intensity Frontier	1
²⁸	0.1 The Liquid Argon Time Projection Chamber Technology	1
²⁹	0.1.1 TPCs, Neutrinos & Argon	1
³⁰	0.1.2 LArTPC: Principles of Operation	5
³¹	0.1.3 Liquid Argon: Ionization Charge	6
³²	0.1.4 Liquid Argon: Scintillation Light	12
³³	0.1.5 Signal Processing and Event Reconstruction	16
³⁴	0.2 The Intensity Frontier Program	20
³⁵	0.2.1 Prospects for LArTPCs in Neutrino Physics: SBN and DUNE	20
³⁶	0.2.2 Prospects for LArTPCs in GUT Physics: DUNE	22
³⁷	0.2.3 Enabling the next generation of discoveries: LArIAT	23
³⁸	1 Total Hadronic Cross Section Measurement Methodology	26
³⁹	1.1 Event Selection	27
⁴⁰	1.1.1 Selection of Beamline Events	27
⁴¹	1.1.2 Particle Identification in the Beamline	28
⁴²	1.1.3 TPC Selection: Halo Mitigation	28
⁴³	1.1.4 TPC Selection: Shower Removal	29
⁴⁴	1.2 Beamline and TPC Handshake: the Wire Chamber to TPC Match .	30

45	1.3	The Thin Slice Method	32
46	1.3.1	Cross Sections on Thin Target	32
47	1.3.2	Not-so-Thin Target: Slicing the Argon	33
48	1.3.3	Corrections to the Raw Cross Section	35
49	1.4	Procedure testing with truth quantities	36
50	2	Preparatory Work	38
51	2.1	Cross Section Analyses Data Set	38
52	2.2	Construction of a Monte Carlo Simulation for LArIAT	40
53	2.2.1	G4Beamline	40
54	2.2.2	Data Driven MC	44
55	2.2.3	Estimate of Energy Loss before the TPC	47
56	2.3	Tracking Studies	50
57	2.3.1	Study of WC to TPC Match	51
58	2.3.2	Tracking Optimization	54
59	2.3.3	Angular Resolution	54
60	2.4	Calorimetry Studies	58
61	2.4.1	Energy Calibration	58
62	2.4.2	Kinetic Energy Measurement	60
63	3	Negative Pion Cross Section Measurement	64
64	3.1	Raw Cross Section	64
65	3.1.1	Statistical Uncertainty	65
66	3.1.2	Treatment of Systematics	67
67	3.2	Corrections to the Raw Cross Section	67
68	3.2.1	Treatment of Systematics	67

⁶⁹ Acknowledgements

⁷⁰ “*Dunque io ringrazio tutti quanti.*

⁷¹ *Specie la mia mamma che mi ha fatto così funky.”*

⁷² – Articolo 31, Tanqi Funky, 1996 –

⁷³ “*At last, I thank everyone.*

⁷⁴ *Especiallly my mom who made me so funky.”*

⁷⁵ – Articolo 31, Tanqi Funky, 1996 –

⁷⁶ A lot of people are awesome, especially you, since you probably agreed to read

⁷⁷ this when it was a draft.

⁷⁸ **Chapter 0**

⁷⁹ **Liquid Argon Detectors at the**
⁸⁰ **Intensity Frontier**

⁸¹ In the next few years, LArTPCs will be the tools to answer some of the burning
⁸² questions in neutrino physics today. This section illustrates the operational principles
⁸³ of this detector technology, as well as the scope of the key detectors in the US liquid
⁸⁴ argon program – SBN, DUNE and LArIAT.

⁸⁵ **0.1 The Liquid Argon Time Projection Chamber**
⁸⁶ **Technology**

⁸⁷ **0.1.1 TPCs, Neutrinos & Argon**

⁸⁸ David Nygren designed the first Time Projection Chamber (TPC) in the late 1970s [41]
⁸⁹ for the PEP-4 experiment, a detector apt to study electron-positron collisions at the
⁹⁰ PEP storage ring at the SLAC National Accelerator Laboratory. From the original
⁹¹ design in the seventies – a cylindrical chamber filled with methane gas – the TPC
⁹² detector concept has seen many incarnations, the employment of several different
⁹³ active media and a variety of different particle physics applications, including, but

94 not limited to the study of electron/positron storage rings (e.g. PEP4, TOPAZ,
95 ALEPH and DELPHI), heavy ions collisions in fixed target and collider experiments
96 (e.g. EOS/HISSL and ALICE), dark matter (ArDM), rare decays and capture (e.g.
97 TRIUMF, MuCap), neutrino detectors and nucleon decay (ICARUS, SBN, DUNE),
98 and neutrino less double beta decay (Next). A nice review of the history of TPCs
99 and working principles is provided in [31].

100 Several features of the TPC technology make these detectors a more versatile tool
101 compared to other ionization detectors and explain such a wide popularity. TPCs are
102 the only electronically read detector which deliver simultaneous three-dimensional
103 track information and a measurement of the particle energy loss. Leveraging on both
104 tracking and calorimetry, particle identification (PID) capabilities are enhanced over
105 a wide momentum range.

106 Historically, the active medium in ionization detectors has been in the gaseous
107 form. Carlo Rubbia first proposed the use of a Liquid Argon TPC for a neutrino
108 experiment, ICARUS [46], in 1977. Using nobles elements in the liquid form for
109 neutrino detectors is advantageous for several reasons. The density of liquids is \sim 1000
110 times greater than gases, augmenting the number of targets for neutrino's interaction
111 in the same volume, in a effort to balance the smallness of neutrino cross section.
112 Since the energy loss of charged particle is proportional to the target material density,
113 as shown in the Bethe-Block equation (eq. 1), the increased density reflects into a
114 proportionally higher energy loss, enhancing the calorimetry capability of detectors
115 with a liquid active medium. Additionally, the ionization energy of liquids is smaller
116 than gasses by the order of tens of eV. Thus, at the passage of charged particles,
117 liquids generally produce more ionization electrons than gases for the same deposited
118 energy, forcing the particles to deposit more energy in a shorter range. The downside
119 of using noble liquid elements in experiments is that they require expensive cryogenic
120 systems to cool the gas until it transitions to its the liquid form. The properties

Element	LAr	LXe
Atomic Number	18	54
Atomic weight A	40	131
Boiling Point Tb at 1 atm	87.3 K	165.0 K
Density	1.4 g/cm ³	3.0 g/cm ³
Radiation length	14.0 cm	2.8 cm
Moliere Radius	10.0 cm	5.7 cm
Work function	23.6 eV	15.6 eV
Electron Mobility at $E_{field} = 10^4$ V/m	0.047 m ² /Vs	0.22 m ² /Vs
Average dE/dx MIP	2.1 MeV/cm	3.8 MeV/cm
Average Scintillation Light Yield	40000 γ /MeV	42000 γ /MeV
Scintillation λ	128 nm	175 nm

Table 1: LAr, LXe summary of properties relevant for neutrino detectors.

121 of liquid argon in comparison liquid xenon – a popular choice for dark matter and
 122 neutrinoless double beta decay detectors – are summarized in table 1. Albeit xenon
 123 would be more desirable than argon given some superior properties such as lower
 124 ionization energy and higher density and light yield, argon relative abundance abates
 125 the cost of argon compared to xenon, making argon a more viable choice for the
 126 construction of ton (and kilo-ton) scale neutrino detectors.

127 LArTPCs are some times referred as to “electronic” bubble-chambers, for the
 128 similarity in the tracking and energy resolution which is coupled with an electronic
 129 readout of the imaging information in LArTPCs. Compared to these historic detectors
 130 however, LArTPC bestow tridimensional tracking and a self triggering mechanism
 131 provided by the scintillation light in the liquid argon. An event display of a ν_μ CC
 132 interaction candidate in the MicroBooNE detector is shown in picture 1 to display
 133 the level of spatial details these detectors are capable of; the color scale of the image
 134 is proportional to the energy deposited, hinting to these calorimetry capabilities of
 135 the detectors.

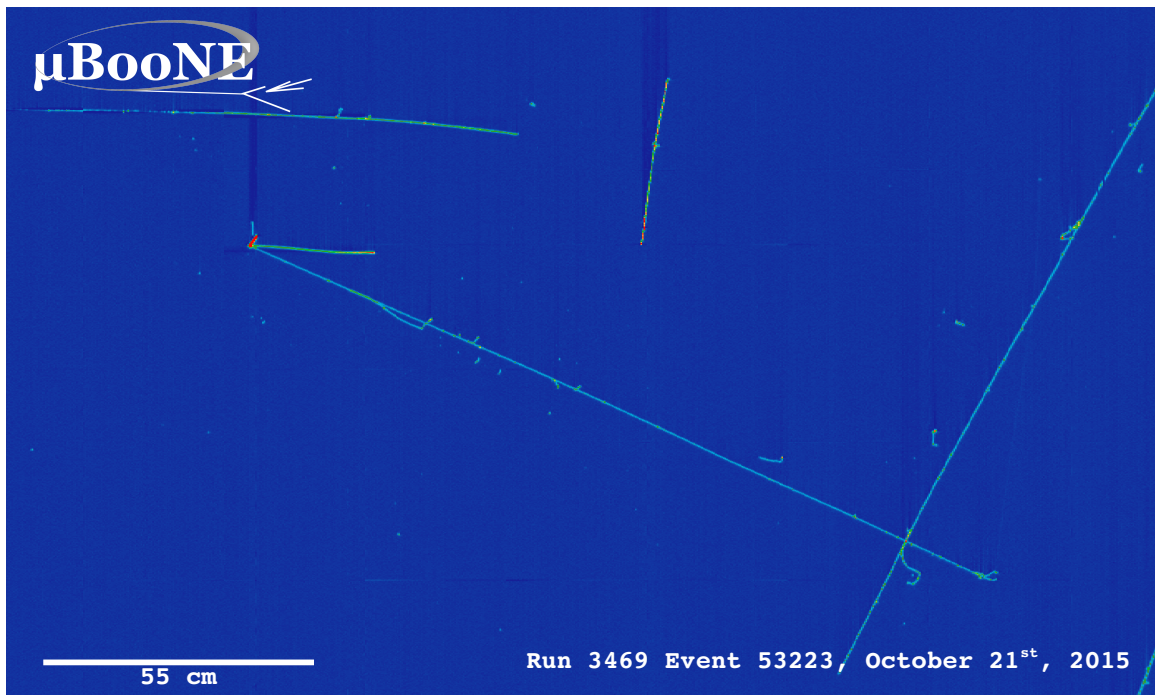


Figure 1: Event display of a ν_μ CC interaction candidate in the MicroBooNE detector.

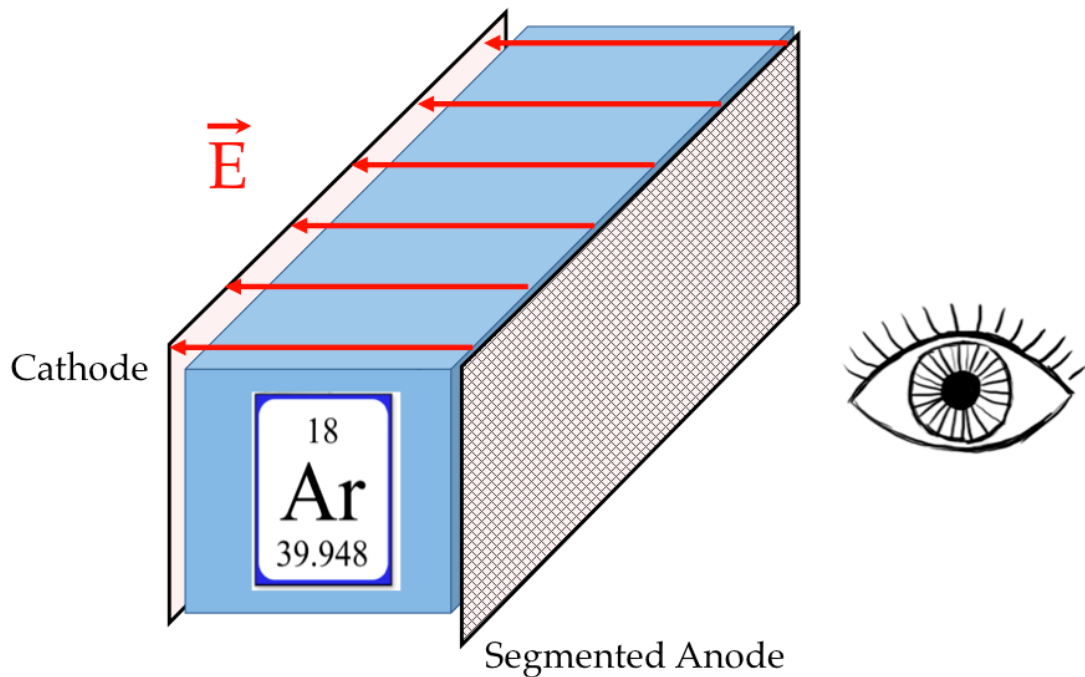


Figure 2: A cartoonish sketch of a LArTPC.

136 **0.1.2 LArTPC: Principles of Operation**

137 To the bare bones, a LArTPC is a bulk of liquid argon sandwiched in a flat capac-
138 itor, equipped with a light collection system, as the cartoon in 2 shows. A uniform
139 electric field of the order of 500 V/cm is maintained constant between the faces of the
140 capacitor. The anode is sensitive to ionization charge and it is usually made of two
141 or more planes segmented into several hundreds parallel sense wires a few millimeters
142 apart; different geometries for the anode segmentation are under study [24].

143 Argon ionization and scintillation are the processes leveraged to detect particles
144 in the LArTPC active volume. When a ionizing radiation traverses the argon active
145 volume it leaves a trail of ionization electrons along its trajectory and it excites
146 the argon producing scintillation light – details on the production and detection of
147 ionization charge and scintillation light are provided in 0.1.4 and 0.1.4 respectively.

148 The optical detector sees the argon scintillation light in matters of nanoseconds.
149 This flash of light determines the start time of an event in the chamber, t_0 . The
150 uniform electric field drifts the ionization electrons from the production point towards
151 the anode in order of hundreds of microseconds or more depending on the chamber
152 dimensions¹. The anode sense wires see either an induced current by the drifting
153 ionization charge (on induction planes) or an injection of such charge (collection
154 plane). An appropriate choice of the voltage bias on each wire plane assures ideal
155 charge transparency, so that all the ionization charge is collected on the collection
156 plane and none on the induction planes.

157 The arrival time of the charge on the anode sense wires is used to measure the
158 position of the original ionizing radiation in the drift direction. In fact, since the
159 constant electric field implies that the drift velocity is also constant, the position of

1. The ionized argon also drifts, but in the opposite directions compared to the electrons. Since the drift time is proportional to the particle mass, the ions' drift time is much longer than the electrons'. Ionized argon is collected on the cathode which is not instrumented, so it is not used to infer information about the interactions in the chamber.

160 the original ionization is simply given by the multiplication of the drift velocity by the
 161 drift time, where the “drift time” is the difference between t_0 and the charge arrival
 162 time on the wire planes. The spacial resolution on this dimension is limited by the
 163 time resolution of the electronics or by longitudinal diffusion of the electrons. The
 164 spatial information on the different wire planes maps a bi-dimensional projection of
 165 the interaction pattern in the plane perpendicular to the drift direction. The spacial
 166 resolution on this dimension is limited by the transverse electron diffusion in argon
 167 and by the grain of the anode segmentation, i.e. the spacing between the wires in
 168 the sense planes [23]. The off-line combination of the 2-D information on the wire
 169 planes with the timing information allows for the 3D reconstruction of the event in
 170 the chamber.

171 Since the charge deposited by the ionizing radiation is proportional to the de-
 172 posited energy and the charge collected on the sense plane is a function of the de-
 173 posited charge, LArTPCs allow the measurement of the energy deposit in the active
 174 volume. Effects due to the presence of free charge and impurities in the active vol-
 175 ume, such as a finite electron lifetime, recombination and space charge, complicate
 176 the relationship between deposited and collected charge affecting the measurement of
 177 the particle’s energy, as described in the next section.

178 **0.1.3 Liquid Argon: Ionization Charge**

179 The mean rate of energy loss by moderately relativistic elementary charge particles
 180 heavier than electrons is well described by the modified Bethe-Bloch [43] equation

$$-\frac{dE}{dx} = K z^2 \frac{Z}{A} \varrho \frac{1}{\beta^2} \left[\frac{1}{2} \ln \frac{2m_e c^2 \beta^2 \gamma^2 T_{max}}{I^2} - \beta^2 - \frac{\delta}{2} \right], \quad (1)$$

181 where z is the number of unit charge of the ionizing radiation, Z , A and ϱ are the
 182 atomic number, mass number and density of the medium, m_e is the electron mass,

183 $\gamma = \frac{\beta}{\sqrt{1-\beta^2}}$ is the Lorentz factor of the ionizing radiation, T_{max} is the maximum kinetic
 184 energy which can be imparted to a free electron in a single collision, I is the mean
 185 excitation energy on eV, δ is the density correction and $K = 0.307075 \text{ MeV g}^{-1} \text{ cm}^2$ is
 186 a numerical conversion factor. The Bethe-Bloch treats the energy loss by an ionizing
 187 radiation via quantum-mechanical collisions producing ionization or an excitation in
 188 the medium as an uniform and continuous process. The density correction terms
 189 becomes relevant for incident particle with high energy, where screening effects due
 190 to the polarization of the medium by high energy particles occur.

191 Excitation and ionization of the detector medium occur in similar amounts. Since
 192 the ionizing collisions occur randomly, we can parametrize their number k in a segment
 193 of length s along the track with a Poissonian function

$$P(k) = \frac{s^k}{k! \lambda^k} e^{-s/\lambda}, \quad (2)$$

194 where $\lambda = 1/N_e \sigma_i$, with N_e being the electron density of σ_i the ionization cross-
 195 section per electron. About 66% of the ionizing collisions in Argon produce only
 196 a single electron/ion pair [31]; in the other cases, the transferred kinetic energy is
 197 enough for the primary electron to liberate one or more secondary electrons, which
 198 usually stay close to the original pair. Occasionally, electrons can receive enough
 199 energy to be ejected with high energy, forming a so-called “ δ -ray”: a detectable short
 200 track off the particle trajectory, as shown in figure 3. The average number of δ -ray
 201 with energy $E > E_0$ per cm follows the empirical form

$$P(E > E_0) \sim \frac{y}{\beta^2 E_0}, \quad (3)$$

202 where y is an empirical factor depending on the medium (0.114 for gaseous Ar), and
 203 β is v/c .

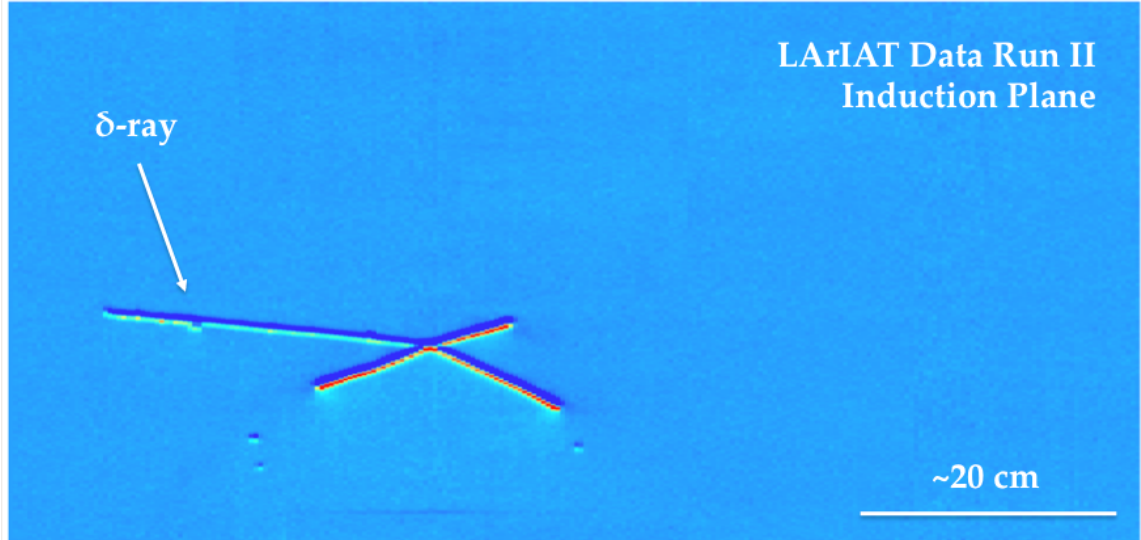


Figure 3: Events display for a LArIAT pion absorption candidate on the induction plane, with highlighted delta ray.

204 Purity & Electron Life Time

205 The presence of electronegative contaminants in liquid argon, such as oxygen O_2
 206 and water H_2O , is particularly pernicious, since these molecules quench the charge
 207 produced by the ionizing radiation. Thus, amount of charge per unit of length dQ/dx
 208 collected on the collection plane depends on the charge's production point in the
 209 detector: ionization produced close to the cathode will see more impurities along its
 210 journey to the collection plane than ionization produced close to the anode, resulting
 211 in greater attenuation of its charge. As a result, the amount of charge collected on
 212 the sense wires as a function of the traveled distance follows an exponential decay
 213 trend. The traveled distance is generally measured in terms of drift time and the
 214 characteristic time constant of the exponential decay is called electron lifetime τ_e .
 215 Figure 4 shows the typical life time for LArIAT data. The procedure to measure
 216 the electron lifetime in LArIAT is outlined in [45]. LArIAT small drift distance (47
 217 cm) allows for a relatively short electron life time. The life time for bigger detectors
 218 such as MicroBooNE, whose drift distance is 2.6 m, needs to be of the order of
 219 tens of milliseconds to allow a charge collection usable for physics analyses. Energy

reconstruction in LArTPC applies a correction for the finite lifetime to calibrate the detector calorimetric response; details for LArIAT are provided in Section 2.4.1.

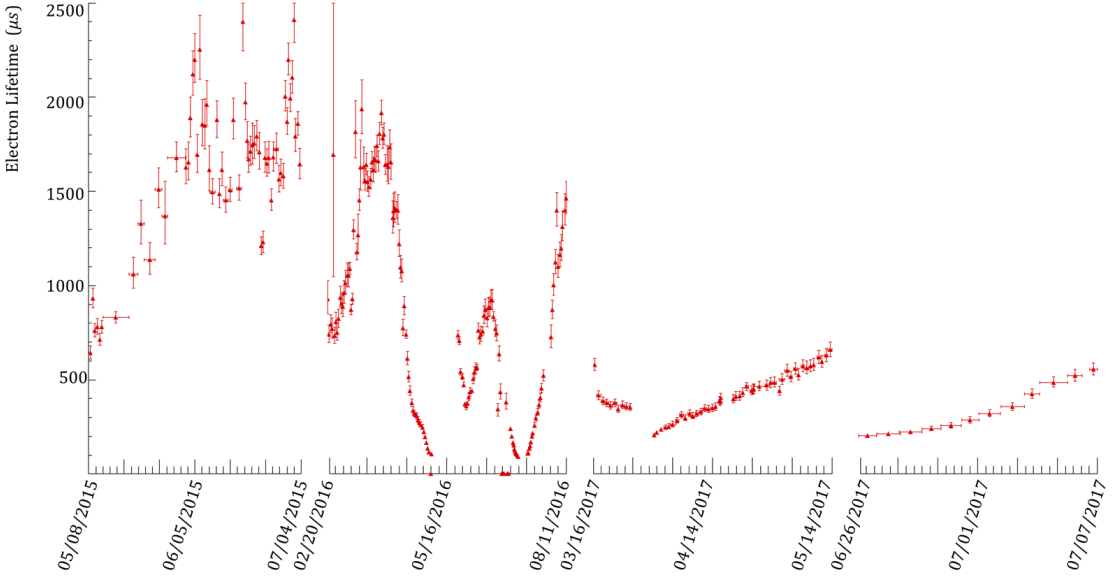


Figure 4: Electron lifetime during the LArIAT run period [22].

LArTPCs use hermetically sealed and leak-checked vessels to abate the leakage and diffusion of contaminants into the system. The liquid argon filling of the volume occurs after the vessel is evacuated or purged with gaseous argon [6] to reduce remaining gases in the volume. Even so, the construction of a pure tank of argon is unviable, as several sources of impurity remain. In particular, impurities can come from the raw argon supply, the argon filtration system and from the outgassing from internal surfaces. Outgassing is a continuous diffusive process producing contaminants, especially water, even after the vessel is sealed, particularly from materials in

230 the ullage region². Since research-grade argon comes from the industrial distillation
231 of air, the impurities with the highest concentration are nitrogen, oxygen and water,
232 generally maintained under the 1 part per million level by the vendor. Even so, a
233 higher level of purity is necessary to achieve a free electron life time usable in meter
234 scale detectors. Thus, argon is constantly filtered in the cryogenic system, which
235 reduce the oxygen and water contamination to less than 100 parts per trillion. The
236 filtration system depends on the size and drift distance of the experiment and, for
237 experiments on several meters scale, it includes an argon recirculation system.

238 Recombination Effect

239 After production, ionization electrons thermalize with the surrounding medium and
240 may recombine with nearby ions. Recombination might occur either between the
241 electron and the parent ion through Coulomb attraction, as described in the geminate
242 theory [42], or thanks to the collective charge density of electrons and ions from
243 multiple ionizations in a cylindrical volume surrounding the particle trajectory, as
244 described in the columnar model [34]. Consideration on the average electron-ion
245 distance and the average ion-ion distance for argon show that the probability of
246 geminate recombination is low; thus recombination in argon is mainly due to collective
247 effects [2]. Since protons, kaons and stopping particles present a higher ionization
248 compared to MIPs, recombination effects are more prominent when considering the
249 reconstruction of energy deposited by these particles.

250 Theoretical descriptions of recombination based on the Birks model and the Box
251 model are provided in [18] and [48], respectively. The Birks model assumes a gaussian
252 spatial distribution around the particle trajectory during the entire recombination
253 phase and identical charge mobility for ions and electrons. The Box model also as-

2. While the liquid argon low temperature reduces outgassing in the liquid, this process remains significant for absorptive material (such as plastic) above the surface of the liquid phase.

sumes that electron diffusion and ion mobility are negligible in liquid argon during recombination. In these models, the fraction of ionization electrons surviving recombination is a function of the number of ion-electron pairs per unit length, the electric field, the average ion-electron separation distance after thermalization and the angle of the particle with respect to the direction of the electric field – plus the diffusion coefficient in the Birks model. Given the stringent assumptions, it is perhaps not surprising that these models are in accordance to data only in specific regimes: the Birks model is generally used to describe recombination for low dE/dx , the Box model for high dE/dX . In LArTPC, the ICARUS and ArgoNeut experiments have measured recombination in [11] and [2] respectively. Since LArIAT uses the refurbished ArgoNeut TPC and cryostat at the same electric field, LArIAT currently corrects for recombination using the ArgoNeut measured recombination parameters in [2].

Space Charge Effect

Slow-moving positive argon ions created during ionization can build-up in LArTPC, causing the distortion of the electric field within the detector. This effect, called “space charge effect” leads to a displacement in the reconstructed position of the signal ionization electrons. In surface LArTPCs the space charge effect is primarily due to the rate of ionization produced by cosmic rays which is slowly drifting in the chamber at all times. Surface LArTPC of the size of several meters are expected to be modestly impacted from the space charge effect, where charge build-up create anisotropy of the electric field magnitude of the order of 5% at a drift field of 500 V/cm [39]. The smallness of the LArIAT drift volume and its relatively high electric field are such that the effect of space charge is expected to be negligible.

²⁷⁷ **0.1.4 Liquid Argon: Scintillation Light**

²⁷⁸ Liquid argon emits scintillation light at the passage of charged particles. LArTPCs
²⁷⁹ leverage this property to determine when the ionization charge begins to drift towards
²⁸⁰ the anode plane.

²⁸¹ **Scintillation Process**

²⁸² Scintillation light in argon peaks in the ultraviolet at a 128 nm, shown in comparison
²⁸³ to Xenon and Kypton in Figure 5, from [40]. The light yield collected by the optical
²⁸⁴ detector depends on the argon purity, the electric field, the dE/dx and particle type,
²⁸⁵ averaging at the tens of thousands of photons per MeV.

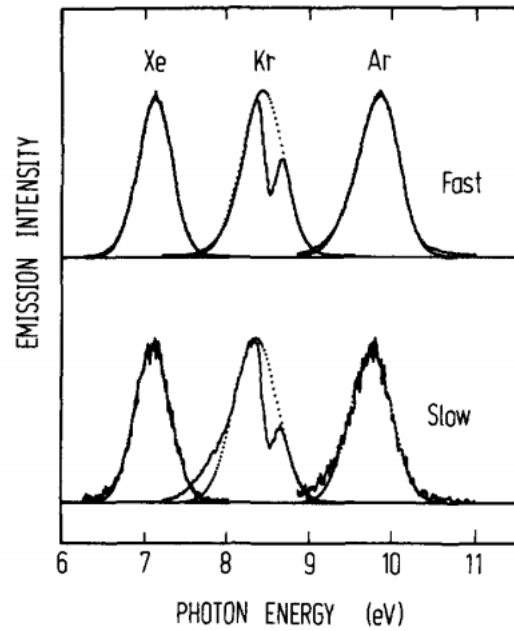


Figure 5: Emission spectra of the fast and slow emission components in Xenon, Krypton and Argon according to [40]. The dotted lines correspond to the Gaussian fits.

²⁸⁶ The de-excitation of Rydberg dimers in the argon is responsible for the scintillation
²⁸⁷ light. Rydberg dimers exist in two states: singlets and a triplets. The time constant
²⁸⁸ for the singlet radiative decay is 6 ns, resulting in a prompt component for the scin-

tillation light. The decay of the triplet is delayed by intersystem crossing, producing a slow component with a time constant of ~ 1500 ns. “Self-trapped exciton luminescence” and “recombination luminescence” are the two processes responsible for the creation of the Rydberg dimers [36]. In the first process, a charged particle excites an argon atom which becomes self-trapped in the surrounding bulk of argon, forming a dimer; the dimer is in the singlet state 65% of the times and in the triplet state 35% of the times. In case of recombination luminescence, the charged particle transfers enough energy to ionize the argon. The argon ion forms a charged argon dimer state, which quickly recombines with the thermalized free electron cloud. Excimer states are produced in the recombination, roughly half in the singlet and half in the triplet state. The light yield dependency on the electric field, on the dE/dx and particle type derives from the role of free charge in the recombination luminescence process. The spacial separation between the argon ions and the free electron cloud depends on the electric field. On one hand, a strong electric field diminishes the recombination probability, leading to a smaller light yield; on the other, it increases the free charge drifting towards the anode plane. Hence, the amount of measurable charge and light anti-correlates as a function of the electric field. Ionizing particles in the argon modify the local density of both free electrons and ions depending on their dE/dx . Since the recombination rate is proportional to the square of the local ionization density, highly ionizing particles boost recombination and the subsequent light yield compared to MIPs. The possibility to leverage this dependency for pulseshape-based particle identification has been shown in [19,38].

Effects Modifying the Light Yield

The production mechanism through emission from bound excimer states implies that argon is transparent to its own scintillation light. In fact, the photons emitted from these metastable states are not energetic enough to re-excite the argon bulk, greatly

315 suppressing absorption mechanisms. In a LArTPC however, several processes modify
316 the light yield in between the location where light is produced and the optical detector.
317 In a hypothetical pure tank of argon, Rayleigh scattering would be the most important
318 processes modifying the light yield. Rayleigh scattering changes the path of light
319 propagation in argon, prolonging the time between light production and detection.
320 The scattering length has been measured to be 66 cm [32] , shorter than the theoretical
321 prediction of \sim 90 cm [47]; this value is short enough to be relevant for the current
322 size of LArTPCs detectors. In fact, Rayleigh scattering worsen the resolution on t_0 ,
323 the start time for charge drifting, and alters the light directionality, complicating the
324 matching between light and charge coming from the same object in case of multiple
325 charged particles in the detector.

326 Traces of impurities in argon such as oxygen, water and nitrogen also affect the
327 light yield, mainly via absorption and quenching mechanisms. Absorption occurs as
328 the interaction of a 128 nm photon directly with the impurity dissolved in the liquid
329 argon. Differently, quenching occurs as the interaction of an argon excimer and an
330 impurity, where the excimer transfers its excitation to the impurity and dissociates
331 non-radiatively. Given this mechanism, it is evident how quenching is both a function
332 of the impurity concentrations and the excimer lifetime. Since the triplet states
333 live much longer than the singlet states, quenching occurs mainly on triplet states,
334 affecting primarily the slow component of the light, reducing the scintillation yield
335 and a shortening of the scintillation time constants.

336 The stringent constraints for the electron life time limit the presence of oxygen and
337 water to such a low level that both absorption and quenching on these impurity is not
338 expected to be significant. Contrarily, the nitrogen level is not bound by the electron
339 life time constraints – nitrogen being an inert gas, expensive to filter. Thus, nitrogen
340 is often present at the level provided by the vendor. The effects of nitrogen on argon
341 scintillation light have been studied in the WArP R&D program and at several test

342 stands. The quenching process induced by nitrogen in liquid Ar has been measured
343 to be proportional to the nitrogen concentration, with a rate constant of ~ 0.11
344 μs^{-1} ppm $^{-1}$; appreciable decreasing in lifetime and relative amplitude of the slow
345 component have been shown for contamination as high as a few ppm of nitrogen [3].
346 For a nitrogen concentration of 2 parts per million, typical of the current generation
347 of LArTPC, the attenuation length due to nitrogen has been measured to be ~ 30
348 meters [35].

349 **Wavelength Shifting of LAr Scintillation Light**

350 Liquid argon scintillation light is invisible for most optical detectors deployed in a
351 LArTPC, such as cryogenic PMTs and SiPMs, since a wavelength of 128 nm is gen-
352 erally too short to be absorbed from most in glasses, polymers and semiconductor
353 materials. Research on prototype SiPMs absorbing directly VUV light and their
354 deployment in noble gasses experiment is ongoing but not mature [49]. Thus, ex-
355 periments need to shift the wavelength of scintillation light to be able to detect it.
356 Albeit deployed in different ways, neutrinos and dark matter experiments commonly
357 use 1,1,4,4-tetraphenyl-butadiene (TPB) to shift the scintillation light. TPB absorbs
358 the vacuum ultraviolet (VUV) light and emits in the visible at ~ 425 nm [20], with
359 a ratio of visible photon emitted per VUV photon absorbed of $\sim 1.2:1$ [28].

360 Neutrino experiments typically coat their optical detector system evaporating a
361 layer of TPB either directly on the PMTs glass surface or on acrylic plates mounted in
362 front of the PMTs [26]; this technique allows the fast detection light coming directly
363 from the neutrino interaction. Dark matter experiments typically evaporate TPB on
364 reflective foils mounted on the inside walls of the sensitive volume and detect the
365 light after it has been reflected; this technique leads to a higher and more uniform
366 light yield, though scattering effects for both the visible and VUV light augment
367 the propagation time and hinder directionality information [27]. In order to take

368 advantage of both these techniques, hybrid systems with PMT coating and foils are
369 being considered for the next generation of large neutrino detectors.

370 0.1.5 Signal Processing and Event Reconstruction

371 In this section we illustrate the processing and reconstruction chain of the TPC sig-
372 nals, from the pulses on the sense wire to the construction of three dimensional objects
373 with associated calorimetry. Different experiments can chose different software pack-
374 ages for their off line signal processing and event reconstruction, but a popular choice
375 for US based LArTPCs is LArSoft [21]. Based on the Art framework [30], LArSoft is
376 an event-based toolkit to perform simulation, analysis and reconstruction of LArT-
377 PCs events.

378

379 LArTPC signal processing develops in several consecutive stages that we summa-
380 rize here in the following categories: *Deconvolution*, *Hit Reconstruction*, *2D Cluster-*
381 *ing*, *3D Tracking*, *Calorimetry Reconstruction*. A visualization of the signal processing
382 workflow is shown in figure 6.

383

384 **Deconvolution.** Induction and collection planes have different field responses,
385 given the different nature of the signals on these planes: the wires on the induction
386 planes see the inductive signal of the drifting charge, while the wires on the collection
387 planes see the current derived from the charge entering the conductor. Thus, signals
388 on the induction plane are bi-polar pulse and signal on the collection plane are unipo-
389 lar pulses, see Figure 6 panel a). The first step in signal processing is deconvolution,
390 that is a series of off-line algorithms geared towards undoing the detector effects. The
391 result of the deconvolution step is the production of a comparable set waveforms on
392 all planes presenting unipolar, approximately gaussian-like pulses (Figure 6 panel b).
393 Signal from all planes are treated on equal footage beyond this point. Some LArTPC

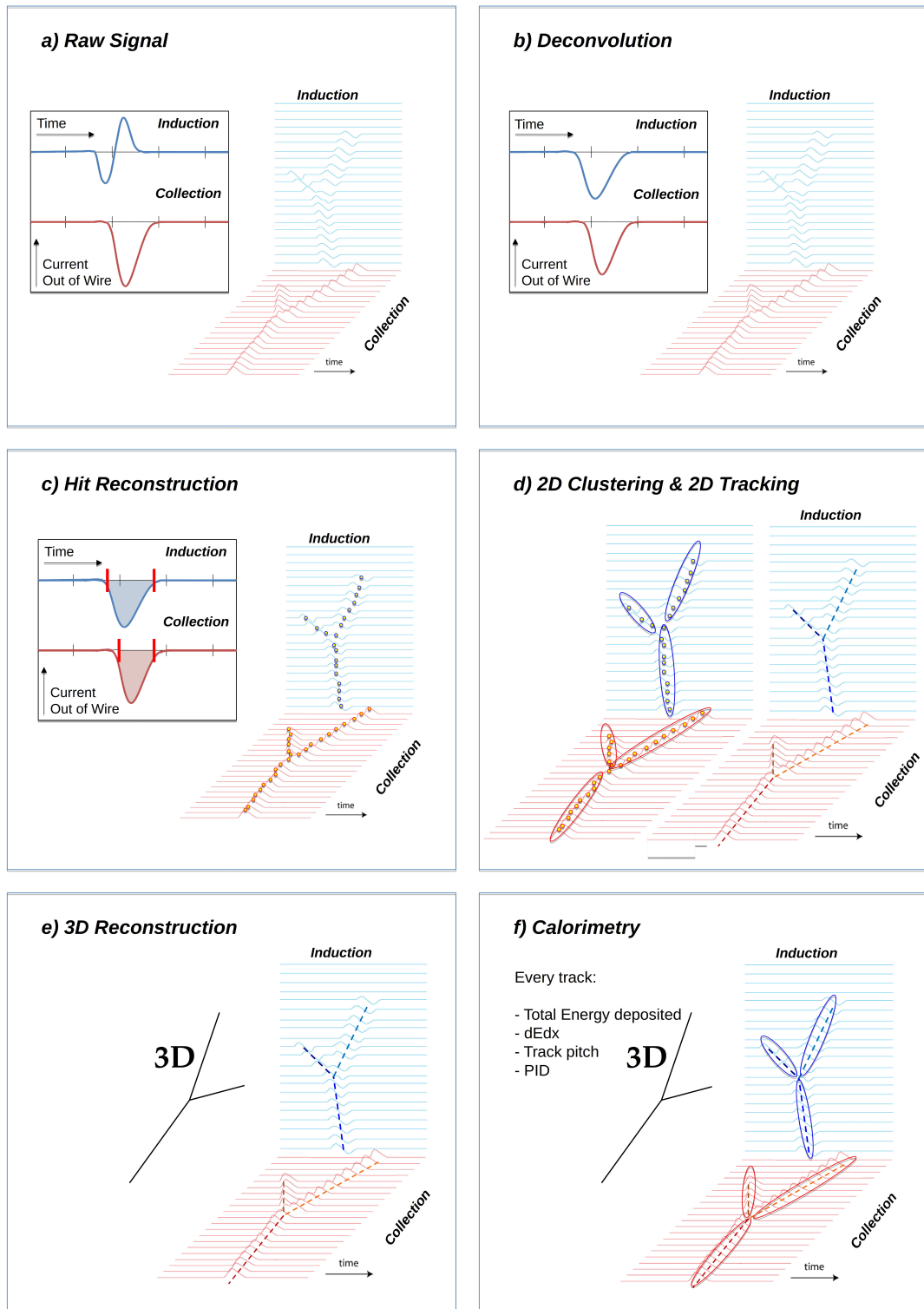


Figure 6: A scheme of a typical signal processing workflow in LArSoft.

394 apply noise filtering in the frequency domain just after the deconvolution to clean
395 up wire cross talk. Since signals from the LArIAT TPC are extremely clean, noise
396 filtering is not necessary.

397

398 **Hit Reconstruction.** The second stage of the signal processing is the recon-
399 struction of hits, indicating an energy deposition in the detector. A peak finder scans
400 the deconvolved TPC waveforms for each wire on the whole readout time looking for
401 spikes above the waveform’s baseline. It then fits these peaks with gaussian shapes
402 and stores the fit parameters such as the quality of the fit, the peak time, height
403 and area under the gaussian fit. The information resulting from this process on a
404 single spike form a single reconstructed “hit”, see Figure 6 panel c). The next steps
405 in the event reconstruction chain will then decide if rejecting hits with poor fits. It
406 is important to notice how the height and width of the hit depend on the topology
407 of the event: for example, a particle running parallel to the wire planes will leave
408 a series of sharp hits on many consecutive wires, while a particle traveling towards
409 the planes will leave a long, wide hit on very few wires. The height of the hits and
410 their integral is proportional to the charge collected on the wire, so it depends on the
411 particle type.

412

413 The event reconstruction chain uses collection of hits to form more complex objects
414 associated with the particles in the detector. The development of different approaches
415 to accomplish this task is an extremely hot topic in LArTPC event reconstruction
416 which spans from more traditional approaches such as line-clustering [17] to the use of
417 machine learning tools [25]. Generally speaking, the scope of hit clustering and event
418 reconstruction to provide shower-like or track like-objects with an associated energy
419 reconstruction. This is because different particles have different topology in the de-
420 tector – electrons and photon create electromagnetic showers, resulting in shower-like

421 topologies, while muons and hadrons leave track-like signals. For the scope of these
422 thesis, we will describe only LArIAT's approach to track reconstruction even if we
423 recognize the breath of LArTPC event reconstruction is much wider. We are inter-
424 ested in the reconstruction of pions and kaons in the active volume, whose topology
425 is track-like.

426

427 **2D Clustering Reconstruction.** The LArIAT reconstruction of track-like ob-
428 jects starts by clustering hits on the collection and induction planes separately with
429 the use of the TrajCluster clustering package [16]. TrajCluster looks for a collection
430 of hits in the wire-time 2D space which can be described with a line-like 2D trajec-
431 tory. TrajCluster reconstructs trajectories by adding trajectory points to the leading
432 edge of the trajectory while stepping through the 2D space of hits. Several factors
433 determine whether a hit is added to the trajectory, including but not limited to

- 434 1. the goodness of the fit of the single hit,
435 2. the charge of the hit compared to the average charge and RMS of the hits
436 already forming the trajectory,
437 3. the goodness of trajectory fit with and without the hit addition,
438 4. the angle between the two lines formed by the collection of hits before and after
439 the considered hit in the trajectory.

440 The final product of this reconstruction stage is the collection of bidimensional clusters
441 on each wire plane, see Figure 6 panel d).

442 **3D Tracking.** The 3D tracking set of algorithms uses clusters close in time on
443 the induction and collection planes as starting point to form a 3D track. Firstly, it
444 construct a tentative 3D trajectory using the edges of the clusters. Then, it projected
445 back the tentative trajectory on to the planes and adjusts the parameters of the 3D

446 track fit such that they minimize the distance between the fit projections and the
447 track hits in all wire planes simultaneously. Tridimensional tracking can use multiple
448 clusters in one plane, but it can never break them in smaller groups of hits. This
449 algorithm was first developed for the ICARUS collaboration [13]. The final product
450 of this reconstruction stage is the formation of tridimensional objects in the TPC
451 active volume, see Figure 6 panel e).

452

453 **Calorimetry.** The last step in the event reconstruction chain is to assign calorimetric
454 information to the track (or shower) objects. Calorimetry is performed separately on the different planes. A multi-step procedure is needed to retrieve the energy
455 deposited in the TPC from the charge seen by the wires. For each hit associated with
456 the track object, the calorimetry algorithms calculate the charge seen on every wire
457 using the area underneath the gaussian fit; then, they correct this raw charge by the
458 electron life time, the electronic noise on the considered wire and the recombination
459 effect. Lastly an overall calibration of the energy, explained in detail in section 2.4.1,
460 is applied and the calorimetric information for the given track is assigned. Even if
461 calorimetry is done in 2D, it benefits from the 3D tracking information; typical information available after the calorimetric reconstruction are the total energy deposited
462 by the particle and its stopping power dE/dx at each “track pitch”, i.e. at each 2D
463 projection on the wire plane of the 3D trajectory.

466 0.2 The Intensity Frontier Program

467 0.2.1 Prospects for LArTPCs in Neutrino Physics: SBN and 468 DUNE

469 The ArgoNeut experiment [12] initiated the US LArTPC neutrino program. Following
470 the success of this small TPC on the NuMI beam, a wide program of LArTPCs

471 on neutrino beams has flourished. The construction of LArTPCs as near and far
472 detectors at different baseline allows for the exploration of some of the fundamental
473 questions in neutrino physics today illustrated in section ??.

474 The Short-Baseline Neutrino (SBN) [14] program at Fermilab is tasked with con-
475 clusively assess the nature of the “LSND and MiniBooNE anomalies” [9, 10, 15], re-
476 solving the mystery of sterile neutrinos at the eV² scale. The SBN program entails
477 three surface LArTPCs positioned on the Booster Neutrino Beam at different dis-
478 tances from the neutrino production in oder to fully exploit the L/E dependence of
479 the oscillation pattern: SBND (100 m from the decay pipe), MicroBooNE (450 m),
480 and ICARUS (600 m). Within the oscillation context, the choice of the LArTPC tech-
481 nology for the SBN detectors changes the set of systematics with respect to LSND
482 and MiniBooNE, whose detection techniques were both based on Cherenkov light.
483 In particular, LArTPCs provide excellent electron/photon separation [5] lacking in
484 Cherenkov detectors which can be leveraged to abate the photon background from
485 neutral current interactions in ν_e searches. MicroBooNE [4], the first detector of
486 the SBN program to be fully operational, started its first neutrino run in October
487 2015. MicroBooNE is a 89 ton active volume LArTPC, single drift chamber with
488 TPC dimensions of 2.6 m (drift) x 2.3 m (heigh) x 10.4 m (depth). MicroBooNE is
489 positioned at a very similar L/E on the Booster neutrino beam as MiniBooNE has
490 the scope to directly cross check the MiniBooNE oscillation measurement. In case
491 MicroBooNE confirms the presence of the “low energy excess” anomaly, SBND and
492 ICARUS will provide the full measurement of the oscillation parameters. SBND and
493 ICARUS are both dual drift chambers, whose active volume is respectively 112 ton
494 and 600 ton. ICARUS is scheduled to become operational by the end of 2018 and
495 SBND shortly after. Besides the oscillation analysis, the second main goals of SBN is
496 to perform an extensive campaign of neutrino cross section measurements in argon.
497 Given the importance of nuclear effects in (relatively) heavy materials, as discussed in

498 section ??, both the oscillation analysis of the SBN program and the measurements
499 of neutrino properties in DUNE will benefit from such a campaign.

500 On a different neutrino beam and baseline, the DUNE experiment, née LBNE [7],
501 is the flagship experiment on the medium-long term of US-based neutrino physics,
502 scheduled to start data taking in 2026. Shooting neutrinos from Fermilab for 800 miles
503 to the SURF laboratory in South Dakota, DUNE is tasked with performing conclusive
504 measurements of CP violation in the lepton sector, the neutrino mass ordering and
505 the θ_{23} octant. The DUNE far detector will count four 10 kton LArTPCs, roughly of
506 dimensions of 19 m (horizontally) x 18 m (vertically) x 66 m (depth).

507 0.2.2 Prospects for LArTPCs in GUT Physics: DUNE

508 The experimental exploration of a manifestation of Grand Unified Theory is possible
509 in DUNE thanks to its sheer mass. In particular, proton decay searches are a capital
510 topic of DUNE’s wide non-accelerator physics program. The key elements for a
511 rare decay experiment are: massive active volume, long exposure, high identification
512 efficiency and low background. Figure 7 shows the current best experimental limits
513 on nucleon decay lifetime over branching ratio (dots). Historically, the dominant
514 technology used in these searches has been water Cherenkov detectors: all the best
515 experimental limits on every decay mode are indeed set by Super-Kamiokande [?, ?].
516 As shown in section ??, different family of GUTs predict the proton to decay in
517 different modes. In particular, SUSY flavored GUTs prefer the presence of kaons
518 in the decay products, e.g. $p \rightarrow K^+ \bar{\nu}$. It is particularly important to notice that
519 the kaon energy for the proton decay mode $p \rightarrow K^+ \bar{\nu}$ is under Cherenkov threshold
520 in water. Thus, Super-Kamiokande set the limit on the lifetime for the $p \rightarrow K^+ \bar{\nu}$
521 mode by relying on photons from nuclear de-excitation and on the muon tagging in
522 the kaon decay leptonic mode. For this reason, an attractive alternative approach to
523 identifying nucleon decay is the use of a LArTPCs, where the kaon is directly visible

524 in the detector. According to [7], DUNE will have an active volume large enough,
 525 have sufficient shielding from the surface, and will run for lengths of time sufficient
 526 to compete with Hyper-K, opening up the opportunity for the discovery of nucleon
 527 decay.

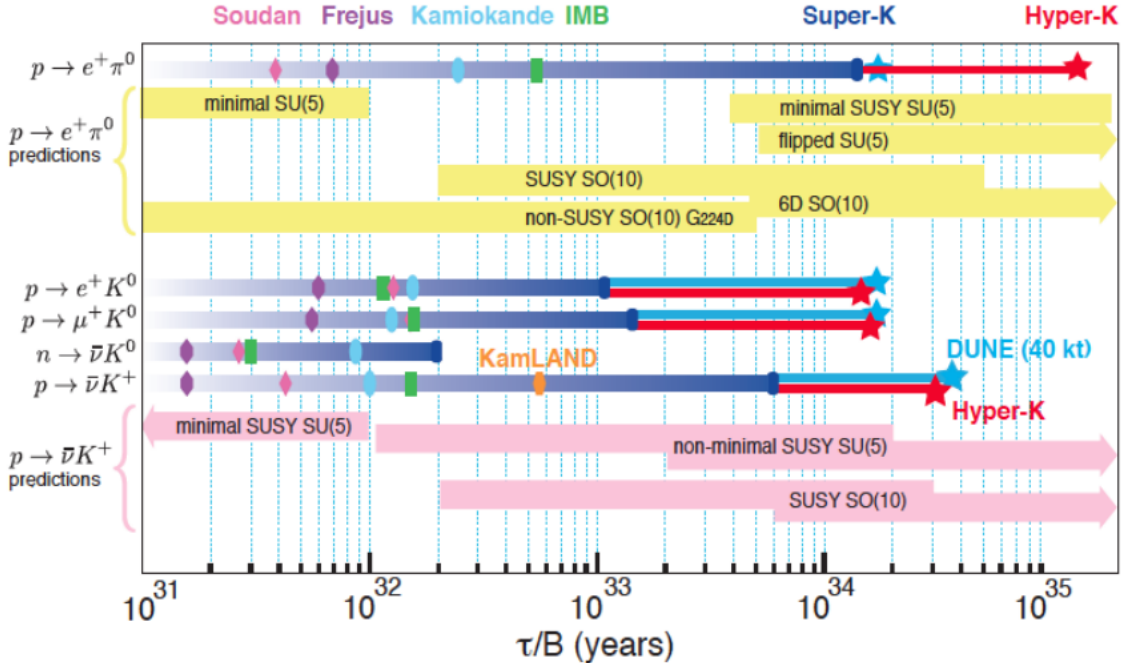


Figure 7: Proton decay lifetime limits from passed and future experiments.

528 0.2.3 Enabling the next generation of discoveries: LArIAT

529 LArIAT, a small LArTPC in a test beam, is designed to perform an extensive physics
 530 campaign centered on charged particle cross section measurements while characteriz-
 531 ing the detector performance for future LArTPCs. Since LArTPCs represent the most
 532 advanced experiments for physics at the Intensity Frontier, their complex technology
 533 needs a thorough calibration and dedicated measurements of some key quantities to
 534 achieve the precision required for the next generation of discoveries. LArIAT’s goal
 535 is to provide such calibration and dedicated measurements. The LArIAT LArTPC is
 536 deployed in a dedicated calibration test beamline at Fermilab. We use the LArIAT

beamline to characterize the charge particles before they enter the TPC: the particle type and initial momentum is known from beamline information. The precise calorimetric energy reconstruction of the LArTPC technology enables the measurement of the total differential cross section for tagged hadrons. The Pion-Nucleus and Kaon-Nucleus total hadronic interaction cross section have never been measured before in argon and they are a fundamental step to shed light on light meson interaction in nuclei per se, while providing a key input to neutrino physics and proton decay studies in future LArTPC experiments like SBN and DUNE.

In order to showcase LArIAT’s utility to SBN and DUNE, we illustrate briefly two comparisons as examples: one regarding neutrino interactions and the second regarding proton decay studies.

The left side of figure 8 shows the distribution of products in momentum spectrum and particle type as simulated in a ν_e CC interaction in DUNE (according to [37]); the range of these distribution is to compare with the momentum distribution of light particles in the LArIAT beamline – shown on the right side of figure 8. The momentum spectrum in the LArIAT beamline for electrons, muons and pions – the most abundant particles produced in a ν_e CC interaction – covers a wide range of the expected momentum distribution in a neutrino event.

The signature of a proton decay event in the “LAr golden mode” is the presence of a single kaon of about 400 MeV in the detector; the momentum spectrum of the kaon pre and post FSI in such an event as simulated by GENIE is shown on the left side of figure 9. The right side of figure 9 shows the momentum spectrum of kaons in the LArIAT beamline. Kaons arriving to the LArIAT TPC are ideal for proton decay studies, since their momentum in the beamline is just above the typical momentum for kaons in a proton decay event: the majority of LArIAT kaons slow down in the TPC enough to enter the desired momentum window.

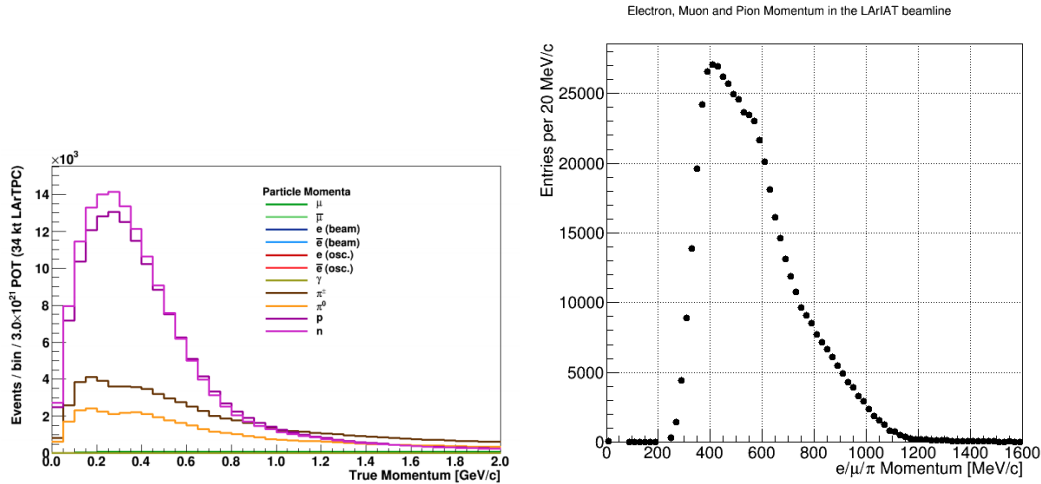


Figure 8: *Left.* Simulation of the products of a ν_e CC interaction in DUNE, both in particles type and momentum.
Right. Momentum spectrum for low mass particles (e, μ, π) in the LArIAT beamline, negative tune, Run II, Picky Tracks see section ??.

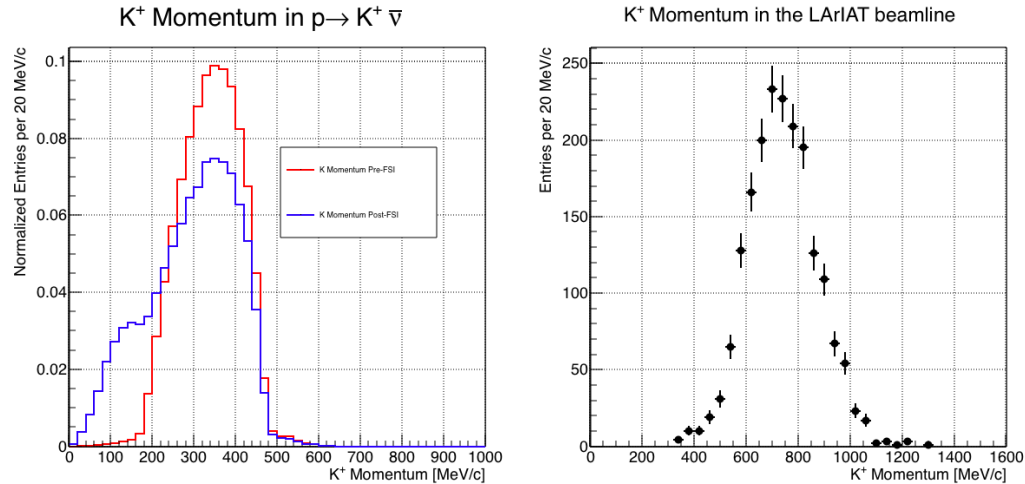


Figure 9: *Left.* Momentum of the kaon outgoing a proton decay $p \rightarrow K^+ \bar{\nu}$ event as simulated by the Genie 2.8.10 event generator in argon. The red line represents the kaon momentum distribution before undergoing the simulated final state interaction inside the argon nucleus, while the blue line represents the momentum distribution after FSI.
Right. Positive Kaon momentum spectrum in the LArIAT beamline, positive tune, Run II, Picky Tracks see section ??.

563 **Chapter 1**

564 **Total Hadronic Cross Section**

565 **Measurement Methodology**

566 This chapter describes the general procedure employed to measure a total hadronic
567 differential cross section in LArIAT. Albeit with small differences, both the (π^- ,Ar)
568 and (K^+ ,Ar) total hadronic cross section measurements rely on the same procedure
569 described in details in the following sections. We start by selecting the particle of
570 interest using a combination of beamline detectors and TPC information (Section
571 ??). We then perform a handshake between the beamline information and the TPC
572 tracking to assure the selection of the right TPC track (Section 1.2). Finally, we apply
573 the “thin slice” method and measure the “raw” hadronic cross section (Section 1.3).
574 A series of corrections are then evaluated to obtain the “true” cross section (Section
575 1.3.3).

576 At the end of this chapter, we show a sanity check of the methodology against
577 MC truth information (Section 1.4).

578 1.1 Event Selection

579 The measurement of the (π^- ,Ar) and (K^+ ,Ar) total hadronic cross section in LArIAT
580 starts by selecting the pool of pion or kaon candidates and measuring their momen-
581 tum. This is done through the series of selections on beamline and TPC information
582 described in the next sections. The summary of the event selection in data is reported
583 in Table 1.1.

584 1.1.1 Selection of Beamline Events

585 As shown in equation 1.5, we leverage the beamline particle identification and mo-
586 mentum measurement before entering the TPC as input to evaluate the kinetic
587 energy for the hadrons used in the cross sections measurements. Thus, we select the
588 LArIAT data to keep only events whose wire chamber and time of flight information
589 is registered (line 2 in Table 1.1). Additionally, we perform a check of the plausi-
590 bility of the trajectory inside the beamline detectors: given the position of the hits
591 in the four wire chambers, we make sure the particle's trajectory does not cross any
592 impenetrable material such as the collimator and the magnets steel (line 3 in Table
593 1.1).

	Run-II Negative Polarity	Run-II Positive Polarity
Events Reconstructed in Beamline	158396	260810
Events with Plausible Trajectory	147468	240954
Beamline $\pi^-/\mu^-/e^-$ Candidate	138481	N.A.
Beamline K^+ Candidate	N.A	2837
Events Surviving Pile Up Filter	108929	2389
Events with WC2TPC Match	41757	1081
Events Surviving Shower Filter	40841	N.A.
Available Events For Cross Section	40841	1081

Table 1.1: Number of data events for Run-II Negative and Positive polarity

594 **1.1.2 Particle Identification in the Beamline**

595 In data, the main tool to establish the identity of the hadron of interest is the LArIAT
596 tertiary beamline, in its function of mass spectrometer. We combine the measurement
597 of the time of flight, TOF , and the beamline momentum, p_{Beam} , to reconstruct the
598 invariant mass of the particles in the beamline, m_{Beam} , as follows

$$m_{Beam} = \frac{p_{Beam}}{c} \sqrt{\left(\frac{TOF * c}{l}\right)^2 - 1}, \quad (1.1)$$

599 where c is the speed of light and l is the length of the particle's trajectory between
600 the time of flight paddles.

601 Figure 1.1 shows the mass distribution for the Run II negative polarity runs on
602 the left and positive polarity runs on the right. We perform the classification of events
603 into the different samples as follows:

- 604 • $\pi/\mu/e$: mass < 350 MeV
605 • kaon: 350 MeV < mass < 650 MeV
606 • proton: 650 MeV < mass < 3000 MeV.

607 Lines 4 and 5 in Table 1.1 show the number of negative $\pi/\mu/e$ and positive K
608 candidates which pass the mass selection for LArIAT Run-II data.

609 **1.1.3 TPC Selection: Halo Mitigation**

610 The secondary beam impinging on LArIAT secondary target produces a plethora of
611 particles which propagates downstream. The presence of upstream and downstream
612 collimators greatly abates the number of particles tracing down the LArIAT tertiary
613 beamline. However, it is possible that more than one particle sneaks into the LArTPC
614 during its readout time: the TPC readout is triggered by the particle firing the

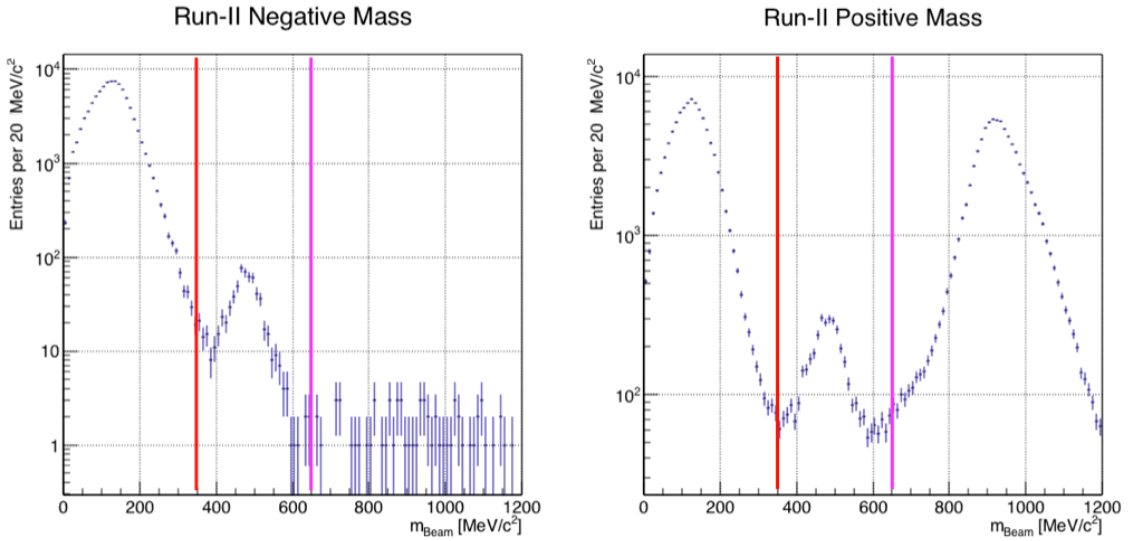


Figure 1.1: Distribution of the beamline mass as calculated according to equation 1.1 for the Run-II events reconstructed in the beamline, negative polarity runs on the left and positive polarity runs on the right. The classification of the events into $\pi^\pm/\mu^\pm/e^\pm$, K^\pm , or (anti)proton is based on these distributions, whose selection cut are represented by the vertical colored lines.

beamline detectors, but particles from the beam halo might be present in the TPC at the same time. We call “pile up” the additional traces in the TPC. We adjusted the primary beam intensity between LArIAT Run I and Run II to reduce the presence of events with high pile up particles in the data sample. For the cross section analyses, we remove events with more than 4 tracks in the first 14 cm upstream portion of the TPC from the sample (line 6 in Table 1.1).

1.1.4 TPC Selection: Shower Removal

In the case of the (π^-, Ar) cross section, the resolution of beamline mass spectrometer is not sufficient to select a beam of pure pions. In fact, muons and electrons survive the selection on the beamline mass. It is important to notice that the composition of the negative polarity beam is mostly pions, as will be discussed in section 2.2.1. Anyhow, we devise a selection on the TPC information to mitigate the presence of

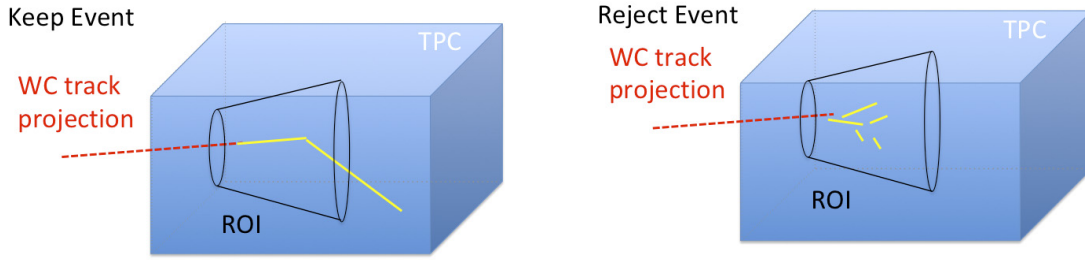


Figure 1.2: Visual rendering of the shower filter. The ROI is a cut cone, with a small radius of 4 cm, a big radius of 10 cm and an height of 42 cm (corresponding to 3 radiation lengths for electrons in Argon).

627 electrons in the sample used for the pion cross section. The selection relies on the
 628 different topologies of a pion and an electron event in the argon: while the former
 629 will trace a track inside the TPC active volume, the latter will tend to “shower”, i.e.
 630 interact with the medium, producing bremsstrahlung photons which pair convert into
 631 several short tracks. In order to remove the shower topology, we create a region of
 632 interest (ROI) around the TPC track corresponding to the beamline particle (more
 633 details on this in the next section). We look for short tracks contained in the ROI, as
 634 depicted in figure 1.4: if more than 5 tracks shorter than 10 cm are in the ROI, we
 635 reject the event. Line 8 in Table 1.1) shows the number of events surviving this
 636 selection.

637 1.2 Beamlne and TPC Handshake: the Wire Cham- 638 ber to TPC Match

639 For each event passing the selection on its beamline information, we need to identify
 640 the track inside the TPC corresponding to the particle which triggered the beamline
 641 detectors, a procedure we refer to as “WC to TPC match” (WC2TPC for short).
 642 In general, the TPC tracking algorithm will reconstruct more than one track in the
 643 event, partially due to the fact that hadrons interact in the chamber and partially

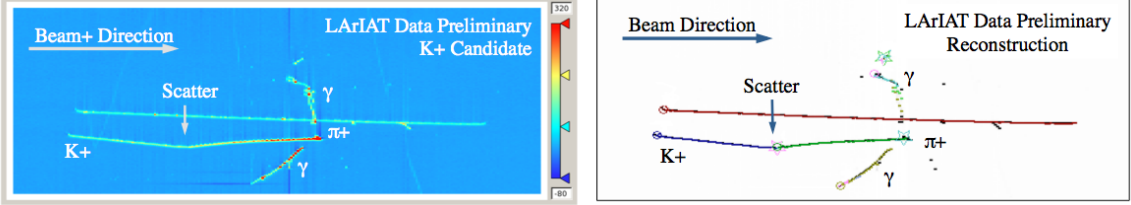


Figure 1.3: Kaon candidate event: on the right, event display showing raw quantities; on the left, event display showing reconstructed tracks. In the reconstructed event display, different colors represent different track objects. A kink is visible in the kaon ionization, signature of a hadronic interaction: the tracking correctly stops at the kink position and two tracks are formed. An additional pile-up track is so present in the event (top track).

644 because of pile up particles during the triggered TPC readout time, as shown in
 645 figure 1.3.

646 We attempt to uniquely match one wire chamber track to one and only one re-
 647 constructed TPC track. In order to determine if the presence of a match, we apply
 648 a geometrical selection on the relative the position of the wire chamber and TPC
 649 tracks. We start by considering only TPC tracks whose first point is in the first 2
 650 cm upstream portion of the TPC for the match. We project the wire chamber track
 651 to the TPC front face where we define the coordinates of the projected point as x_{FF}
 652 and y_{FF} . For each considered TPC track, we define ΔX as the difference between
 653 the x position of the most upstream point of the TPC track and x_{FF} . ΔY is defined
 654 analogously. We define the radius difference, ΔR , as $\Delta R = \sqrt{\Delta X^2 + \Delta Y^2}$. We de-
 655 fine as α the angle between the incident WC track and the TPC track in the plane
 656 that contains them. If $\Delta R < 4$ cm, $\alpha < 8^\circ$, a match between WC-track and TPC
 657 reconstructed track is found. We describe how we determine the value for the radius
 658 and angular selection in sec 2.3.1. In MC, we mimic the matching between the WC
 659 and the TPC track by constructing a fake WC track using truth information at wire
 660 chamber four. We then apply the same WC to TPC matching algorithm as in data.
 661 We discard events with multiple WC2TPC matches. We use only those TPC tracks
 662 that are matched to WC tracks in the cross section calculation.

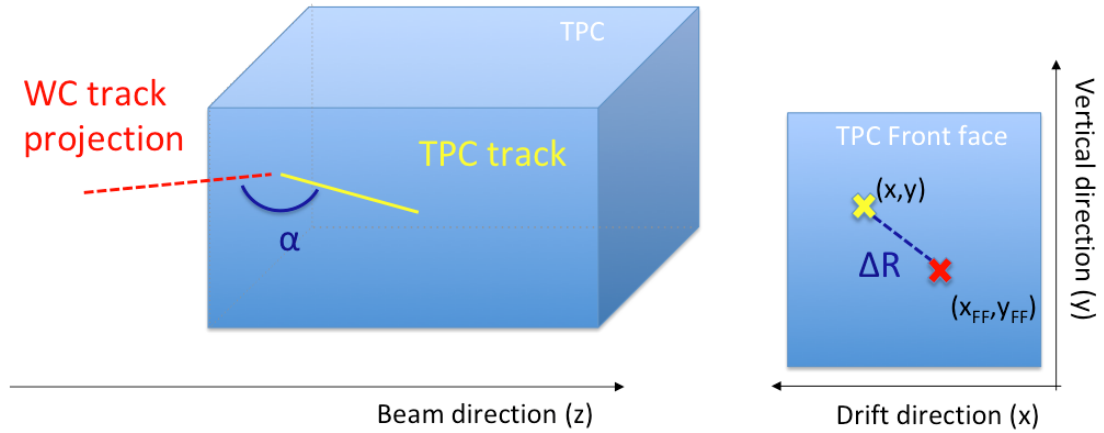


Figure 1.4: Visual rendering of the wire chamber to TPC match.

663 1.3 The Thin Slice Method

664 Once we have selected the pool of hadron candidates and we have identified the TPC
665 track corresponding to the beamline event, we apply the thin slice method to measure
666 the cross section, as the following sections describe.

667 1.3.1 Cross Sections on Thin Target

668 Cross section measurements on a thin target have been the bread and butter of
669 nuclear and particle experimentalists since the Geiger-Marsden experiments [29]. At
670 their core, these types of experiments consist in shooting a beam of particles with a
671 known flux on a thin target and recording the outgoing flux.

672 In general, the target is not a single particle, but rather a slab of material contain-
673 ing many diffusion centers. The so-called “thin target” approximation assumes that
674 the target centers are uniformly distributed in the material and that the target is thin
675 compared to the projectile interaction length, WC2TPC so that no center of interac-
676 tion sits in front of another. In this approximation, the ratio between the number of
677 particles interacting in the target $N_{Interacting}$ and number of incident particles $N_{Incident}$
678 determines the interaction probability $P_{Interacting}$, which is the complementary to one

679 of the survival probability $P_{Survival}$. Equation 1.2

$$P_{Survival} = 1 - P_{Interacting} = 1 - \frac{N_{Interacting}}{N_{Incident}} = e^{-\sigma_{TOT} n \delta X} \quad (1.2)$$

680 describes the probability for a particle to survive the thin target. This formula relates
681 the total cross section σ_{TOT} , the density of the target centers n and the thickness of
682 the target along the incident hadron direction δX , to the interaction probability¹.
683 If the target is thin compared to the interaction length of the process considered,
684 we can Taylor expand the exponential function in equation 1.2 and find a simple
685 proportionality relationship between the number of incident and interacting particles,
686 and the cross section, as shown in equation 1.3:

$$1 - \frac{N_{Interacting}}{N_{Incident}} = 1 - \sigma_{TOT} n \delta X + O(\delta X^2). \quad (1.3)$$

687 Solving for the cross section, we find:

$$\sigma_{TOT} = \frac{1}{n \delta X} \frac{N_{Interacting}}{N_{Incident}}. \quad (1.4)$$

688 1.3.2 Not-so-Thin Target: Slicing the Argon

689 The interaction length of pions and kaons in argon is expected to be of the order
690 of 50 cm for pions and 100 cm for kaons. Thus, the LArIAT TPC, with its 90 cm
691 of length, is not a thin target. However, the fine-grained tracking of the LArIAT
692 LArTPC allows us to treat the argon volume as a sequence of many adjacent thin
693 targets.

694 As described in Chapter ??, LArIAT wire planes consist of 240 wires each. The
695 wires are oriented at +/- 60° from the vertical direction at 4 mm spacing, while the

1. The scattering center density in the target, n , relates to the argon density ρ , the Avogadro number N_A and the argon molar mass m_A as $n = \frac{\rho N_A}{m_A}$.

beam direction is oriented 3 degrees off the z axis in the XZ plane. The wires collect
 signals proportional to the energy loss of the hadron along its path in a $\delta X = 4$
 $\text{mm}/\sin(60^\circ) \approx 4.7 \text{ mm}$ slab of liquid argon. Thus, one can think to slice the TPC
 into many thin targets of $\delta X = 4.7 \text{ mm}$ thickness along the direction of the incident
 particle, making a measurement at each wire along the path.

Considering each slice j a “thin target”, we can apply the cross section calculation
 from Equation 3.1 iteratively, evaluating the kinetic energy of the hadron as it enters
 each slice, E_j^{kin} . For each WC2TPC matched particle, the energy of the hadron
 entering the TPC is known thanks to the momentum and mass determination by the
 tertiary beamline,

$$E_{FrontFace}^{kin} = \sqrt{p_{Beam}^2 - m_{Beam}^2} - m_{Beam} - E_{loss}, \quad (1.5)$$

where E_{loss} is a correction for the energy loss in the dead material between the
 beamline and the TPC front face. The energy of the hadron at each slab is determined
 by subtracting the energy released by the particle in the previous slabs. For example,
 at the j^{th} point of a track, the kinetic energy will be

$$E_j^{kin} = E_{FrontFace}^{kin} - \sum_{i < j} \Delta E_i, \quad (1.6)$$

where ΔE_i is the energy deposited at each argon slice before the j^{th} point as measured
 by the calorimetry associated with the tracking.

If the particle enters a slice, it contributes to $N_{Incident}(E^{kin})$ in the energy bin
 corresponding to its kinetic energy in that slice. If it interacts in the slice, it then
 also contributes to $N_{Interacting}(E^{kin})$ in the appropriate energy bin. The cross section
 as a function of kinetic energy, $\sigma_{TOT}(E^{kin})$ will then be proportional to the ratio
 $\frac{N_{Interacting}(E^{kin})}{N_{Incident}(E^{kin})}$.

717 **1.3.3 Corrections to the Raw Cross Section**

718 Equation 3.1 is a prescription for measuring the cross section in case of a pure beam
 719 of the hadron of interest and 100% efficiency in the determination of the interaction
 720 point. For example, if LArIAT had a beam of pure pions and were 100% efficient
 721 in determining the interaction point within the TPC, the pion cross section in each
 722 energy bin would be given by

$$\sigma^{\pi^-}(E_i) = \frac{1}{n\delta X} \frac{N_{\text{Interacting}}^{\pi^-}(E_i)}{N_{\text{Incident}}^{\pi^-}(E_i)}. \quad (1.7)$$

723 Unfortunately, this is not the case. In fact, the selection used to isolate pions in the
 724 LArIAT beam allows for the presence of some muons and electrons as background.
 725 Also, the LArIAT TPC is not 100% efficient in determining the interaction point.
 726 Therefore we need to apply two corrections evaluated on the MC in order to extract
 727 the cross section from LArIAT data: the background subtraction and the efficiency
 728 correction. Still using the pion case as example, we estimate the pion cross section in
 729 each energy bin changing Equation 1.7 into

$$\sigma^{\pi^-}(E_i) = \frac{1}{n\delta X} \frac{N_{\text{Interacting}}^{\pi^-}(E_i)}{N_{\text{Incident}}^{\pi^-}(E_i)} = \frac{1}{n\delta X} \frac{\epsilon_i^{\text{inc}}[N_{\text{Interacting}}^{\text{TOT}}(E_i) - B_{\text{Interacting}}(E_i)]}{\epsilon_i^{\text{int}}[N_{\text{Incident}}^{\text{TOT}}(E_i) - B_{\text{Incident}}(E_i)]}, \quad (1.8)$$

730 where $N_{\text{Interacting}}^{\text{TOT}}(E_i)$ and $N_{\text{Incident}}^{\text{TOT}}(E_i)$ is the measured content of the interacting
 731 and incident histograms for events that pass the event selection, $B_{\text{interacting}}(E_i)$ and
 732 $B_{\text{Incident}}(E_i)$ represent the contributions from beamline background, and ϵ_i^{int} and ϵ_i^{inc}
 733 are the efficiency corrections for said histograms.

734 As we will show in section ??, the background subtraction for the interacting and
 735 incident histograms can be translated into a corresponding corrections $C_{\text{Interacting}}^{\pi MC}(E_i)$
 736 and $C_{\text{Incident}}^{\pi MC}(E_i)$ and the cross section re-written as follows

$$\sigma^{\pi^-}(E_i) = \frac{1}{n\delta X} \frac{\epsilon_i^{inc}}{\epsilon_i^{int}} \frac{N_{\text{Interacting}}^{\text{TOT}}(E_i)}{N_{\text{Incident}}^{\text{TOT}}(E_i)} \frac{C_{\text{Interacting}}^{\pi MC}(E_i)}{C_{\text{Incident}}^{\pi MC}(E_i)}. \quad (1.9)$$

737 1.4 Procedure testing with truth quantities

738 The (π^-, Ar) and (K^+, Ar) total hadronic cross section implemented in Geant4 can be
 739 used as a tool to validate the measurement methodology. We describe here a closure
 740 test done on Monte Carlo to prove that the methodology of slicing the TPC retrieves
 741 the underlying cross section distribution implemented in Geant4 within the statistical
 742 uncertainty.

743 For pions in the considered energy range, the Geant4 inelastic model adopted to
 744 is “BertiniCascade”, while the elastic model “hElasticLHEP”. For kaons, the Geant4
 745 inelastic model adopted to is “BertiniCascade”, while the elastic model “hElasti-
 746 cLHEP”.

747 For the validation test, we fire about a sample of pions and a sample of kaons
 748 inside the LArIAT TPC active volume using the Data Driven Monte Carlo (see section
 749 2.2.2). We apply the thin-sliced method using only true quantities to calculate the
 750 hadron kinetic energy at each slab in order to decouple reconstruction effects from
 751 issues with the methodology. For each slab of 4.7 mm length along the path of the
 752 hadron, we integrate the true energy deposition as given by the Geant4 transportation
 753 model. Then, we recursively subtracted it from the hadron kinetic energy at the TPC
 754 front face to evaluate the kinetic energy at each slab until the true interaction point is
 755 reached. Since the MC is a pure beam of the hadron of interest and truth information
 756 is used to retrieve the interaction point, no correction is applied. Doing so, we obtain
 757 the true interacting and incident distributions for the considered hadron and we obtain
 758 the true MC cross section as a function of the hadron true kinetic energy.

759 Figure 1.5 shows the total hadronic cross section for argon implemented in Geant4

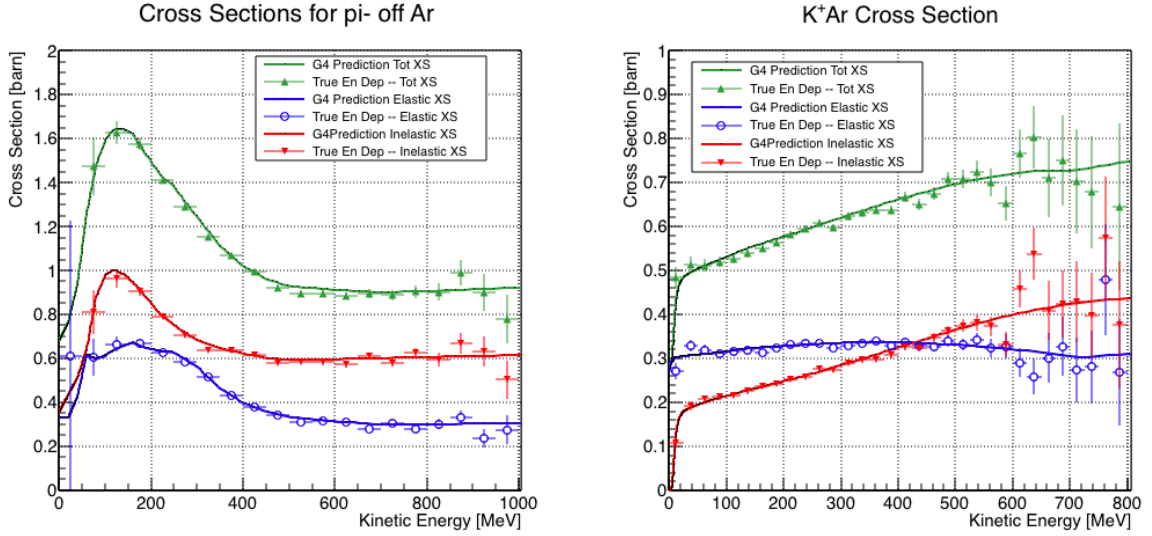


Figure 1.5: Hadronic cross sections for (π^- ,Ar) on the left and (K^+ ,Ar) on the right as implemented in Geant4 10.01.p3 (solid lines) overlaid the true MC cross section as obtained with the sliced TPC method (markers). The total cross section is shown in green, the elastic cross section in blue and the inelastic cross section in red.

760 10.01.p3 (solid lines) overlaid with the true MC cross section as obtained with the
 761 sliced TPC method (markers) for pions on the left and kaons on the right; the total
 762 cross section is shown in green, the elastic cross section in blue and the inelastic
 763 cross section in red. The nice agreement with the Geant4 distribution and the cross
 764 section obtained with the sliced TPC method gives us confidence in the validity of
 765 the methodology.

766 **Chapter 2**

767 **Preparatory Work**

768 This chapter describes the preparatory work done on the the data and Monte Carlo
769 samples used for the cross section analyses. This entails the choice of the data set
770 and the production of the information needed to construct the Monte Carlo Simula-
771 tion (section 2.1), the construction and use of said Monte Carlo simulation (section
772 2.2), the study and optimization of the tracking in the TPC for the cross section
773 analyses (section 2.3), the calibration of the calorimetry response and related energy
774 studies (section 2.4).

775 **2.1 Cross Section Analyses Data Set**

776 We choose LArIAT Run-II as the data period for the (π^-, Ar) and (K^+, Ar) total
777 hadronic cross section analyses. Data taking for the this period started on 03/15/2016
778 and ended on 07/31/2016. Since we are interested in beamline and TPC information,
779 we ask basic requirements on the operational status of the time of fight, wire chambers
780 and TPC to form the good run list for this period, which we informally call “lovely
781 runs”.

782 The subset of lovely runs chosen for the (π^-, Ar) total hadronic cross section
783 analysis includes only the -60A and -100A magnet configurations in negative polarity,

784 even if LArIAT explored several other beamline configurations during Run-II. The
 785 -60A and -100A combined data set accounts for approximately 90% of the total Run-
 786 II negative polarity runs. Since the production of beamline Monte Carlo depends on
 787 the wanted beamline configuration, the choice of only two beamline settings limits
 788 the need for beamline MC production.

789 Similarly, the subset of lovely runs chosen for the (K^+, Ar) total hadronic cross
 790 section analysis includes only the +60A and +100A magnet configurations in positive
 791 polarity. It should be noted that kaons are extremely rare in the +60A sample, thus
 792 the data sample for the (K^+, Ar) cross section after the mass selection is about 90%
 793 +100A runs, as shown in Table 2.1.

794 For the first measurements in LArIAT that uses both beamline and TPC infor-
 795 mation, we choose strict requirements on the reconstruction of the WC tracks, the
 796 so-called “Picky Track” sample (see ??). This choice presents two advantages: the
 797 uncertainty on the momentum reconstruction for the “Picky Tracks” sample is smaller
 798 compared to the “High Yield” sample, and the comparison with the beamline MC
 799 results is straightforward. A possible future update and cross check of these analysis
 800 would be the use of the High Yield sample, where the statistics is about three times
 801 higher.

802 The breakdown of beamline events as a function of the magnets settings is shown
 803 in Table 2.1. The choice of the data sets determines the production of beamline MC
 804 and serves as basis for the production of Data Driven MC, as shown in the next
 805 sections.

	I = 60 A	I = 100 A	Total
Data Events after $\pi/\mu/e$ Mass Selection	67068	71413	138481
Data Events after K Mass Selection	274	2563	2837

Table 2.1: Number of data events which fit the $\pi/\mu/e$ or K mass hypothesis as a function of magnet settings.

806 **2.2 Construction of a Monte Carlo Simulation for**
807 **LArIAT**

808 For the simulation of LArIAT events and their particle make up, we use a combination
809 of two MC generators: the G4Beamline Monte Carlo and the Data Driven single
810 particle Monte Carlo (DDMC). We use the G4Beamline MC to simulate the particle
811 transportation in the beamline and calculate the particle composition of the beam just
812 after the fourth Wire Chamber (WC4). In order to simulate the beamline particles
813 after WC4 and in the TPC, we use the DDMC.

814 **2.2.1 G4Beamline**

815 G4Beamline simulates the beam collision with the LArIAT secondary target, the
816 energy deposited by the particles in the LArIAT beamline detectors, and the action
817 of the LArIAT magnets, effectively accounting for particle transportation through the
818 beam line from the LArIAT target until “Big Disk”, a fictional, void detector located
819 just before the LArIAT cryostat. At the moment of this writing, G4Beamline does
820 not simulated the responses of the beam line detectors. It is possible to interrogate
821 the truth level information of the simulated particles in several points of the geometry.
822 In order to ease the handshake between G4Beamline and the DDMC, we ask for the
823 beam composition just after WC4. Since LArIAT data are taken under different
824 beam conditions, we need to simulate separately the beam composition according to
825 the magnets’ settings and the secondary beam intensity with G4Beamline. For the
826 pion cross section analysis the relevant beam conditions are secondary beam energy
827 of 64 GeV, negative polarity magnet with current of 100 A and 60 A. For the kaon
828 cross section analysis the relevant beam conditions is a secondary beam energy of 64
829 GeV, positive polarity magnet with current of 100 A.

	I = -60 A	I = -100 A
G4Pions	68.8 %	87.4 %
G4Muons	4.6 %	3.7 %
G4Electrons	26.6 %	8.9 %

Table 2.2: Simulated beamline composition per magnet settings

830 Beam Composition for Negative Pion Cross Section

831 Even if pions are by far the biggest beam component in negative polarity runs, the
 832 LArIAT tertiary beam is not a pure pion beam. While useful to discriminate between
 833 pions, kaons, and protons, the beamline detectors are not sensitive enough to discrim-
 834 inate among the lighter particles in the beam: electrons, muons and pions fall under
 835 the same mass hypothesis. Thus, we need to assess the contamination from beamline
 836 particles other than pions in the event selections used for the pion cross section analy-
 837 sis and correct for its effects. The first step of this process is assessing the percentage
 838 of electrons and muons in the $\pi/\mu/e$ beamline candidates via the G4Beamline MC.
 839 The full treatment of the beamline contamination in the pion cross section calculation
 840 is described in section ???. Since the beamline composition is a function of the magnet
 841 settings, we simulate separately events for magnet current of -60A and -100A. Figure
 842 2.1 shows the momentum predictions from G4Beamline overlaid with data for the
 843 60A runs (left) and for the 100A runs (right). The predictions for electrons, muons
 844 and pions have been staggered and their sum is area normalized to data. Albeit not
 845 perfect, these plots show a reasonable agreement between the momentum shapes in
 846 data and MC. We attribute the difference in shape to the lack of simulation of the
 847 WC efficiency in the MC which is momentum dependent and leads to enhance the
 848 number events in the center of the momentum distribution.

849 Table 2.2 shows the beam composition per magnet setting after the mass selection
 850 according to the G4Beamline simulation.

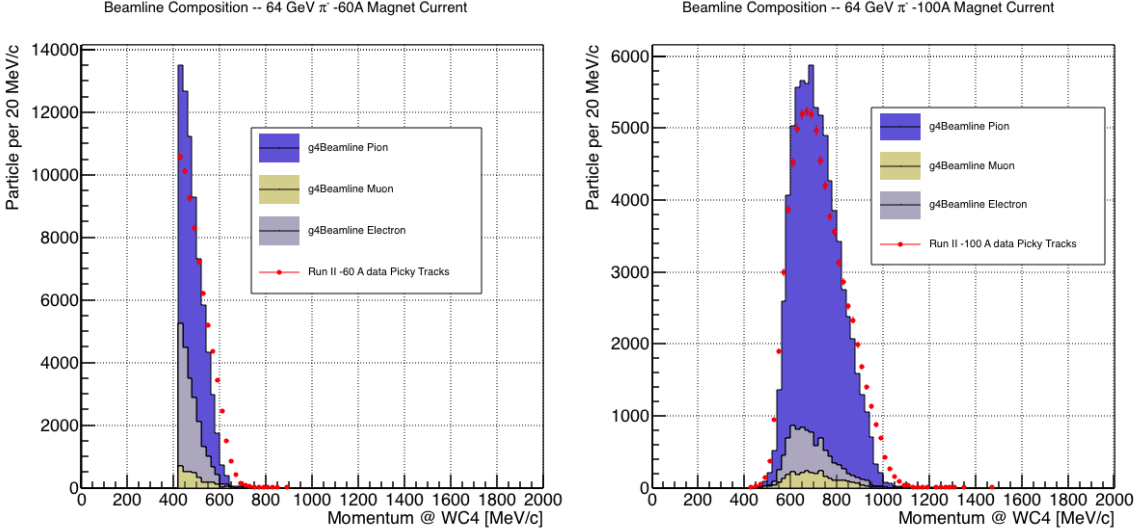


Figure 2.1: Beam composition for the -60A runs (left) and -100A runs (right). The solid blue plot represents the simulated pion content, the yellow plot represents the simulated muon content and the grey plot represents the simulated electron content. The plots are area normalized to the number of data events, shown in red.

851 Beam Composition for Positive Kaon Cross Section

852 In the positive polarity runs, the tertiary beam composition is mainly pions and pro-
 853 tons. The left side of Figure 2.2 shows the predictions for the momentum spectra
 854 for the 100A positive runs according to G4Beamline (solid colors) overlaid with data
 855 (black points). Since the LArIAT beamline detectors can discriminate between kaons
 856 and other particles, we do not rely on the G4Beamline simulation to estimate the
 857 beamline contamination in the pool of kaon candidates (as in the case of the pion
 858 cross section), but rather we use a data driven approach. The basic idea of this data
 859 driven approach is to estimate the bleed over from high and low mass peaks under the
 860 kaon peak by fitting the tails of the $\pi/\mu/e$ and proton mass distributions, as shown
 861 in Figure 2.2 right side. Since the shape of the tails is unknown, the estimate is done
 862 multiple times varying the range and shape for reasonable functions. For example, to
 863 estimate the proton content under the kaon peak, we start by fitting the left tail of
 864 the proton mass distribution with a gaussian function between $650 \text{ MeV}/c^2$ and 750

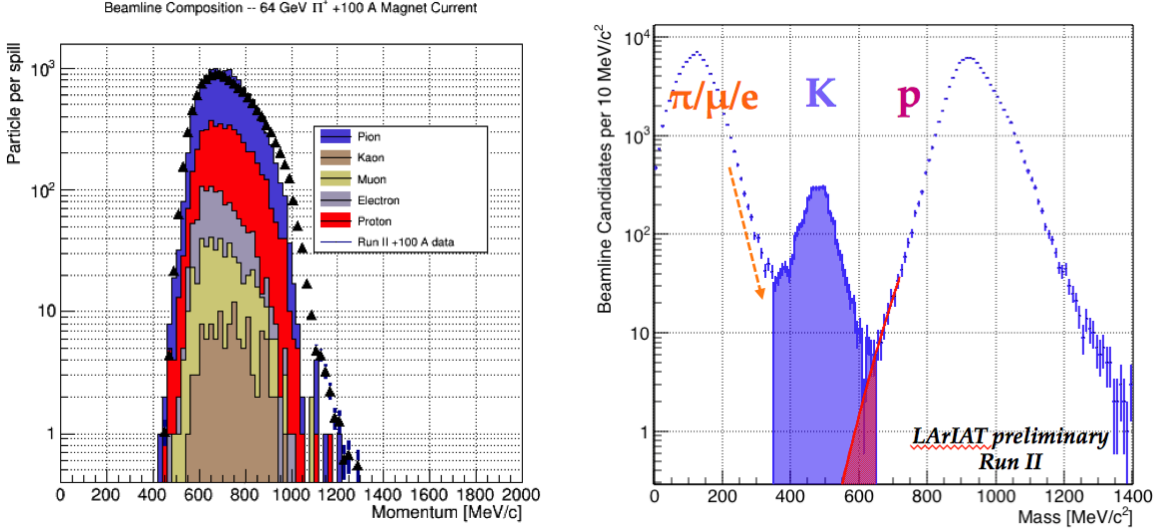


Figure 2.2: *Left.* Beam composition for the +100A runs after WC4 (no mass selection applied). The solid blue plot represents the simulated pion content, the yellow plot represents the simulated muon content and the grey plot represents the simulated positron content, the red the proton content and the mustard the kaon content. The plots are area normalized to the number of data events, shown in black.*Right.* Mass distribution for the Run-II positive runs, where the area under the kaon mass peak is highlighted in purple. The area under the extension of a possible fit for the proton tail is highlighted in red.

865 MeV/c^2 . We extend the fit function under the kaon peak and integrate the between
 866 350-650 MeV/c^2 . We integrate the mass histogram in the same range and calculate
 867 the proton contamination as the ratio between the two integrals. We repeat this pro-
 868 cedure for several fit shapes (gaussian, linear and exponential functions are used) and
 869 tail ranges. Finally, we calculate the contamination as the weighted average of single
 870 estimates, where the weights are calculated to be the $1./\chi^2$ of the tail fits. The pro-
 871 cedure is repeated for lighter particles mass peak independently. With 12 iterations
 872 of this method we find a proton contamination of $0.2 \pm 0.5 \%$ and a contamination
 873 from the lighter particles of $5 \pm 2 \%$.

874 **2.2.2 Data Driven MC**

875 The Data Driven single particle Monte Carlo (DDMC) is a single particle gun which
876 simulates the particle transportation from WC4 into the TPC leveraging on the beam-
877 line data information. The DDMC uses the data momentum and position at WC4
878 to derive the event generation: a general sketch of the DDMC workflow is shown in
879 Figure 2.3.

880 When producing a DDMC sample, beam line data from a particular running pe-
881 riod and/or running condition are selected first. For example, data for the negative
882 60A runs and for the negative 100A runs inform the event generation stage of two
883 different DDMC samples. Figure 2.4 schematically shows the data quantities of in-
884 terest leveraged from data: the momentum (P_x, P_y, P_z) and position (X, Y) at WC4.
885 For each data event, we obtain the particle position (X, Y) at WC4 directly from the
886 data measurement; we calculate the components of the momentum using the beamline
887 measurement of the momentum magnitude in conjunction with the hits on WC3 and
888 WC4 to determine the direction of the momentum vector, as described in section ???.
889 The momentum and position of the selected data form a 5-dimensional tuple, which
890 we sample thousands of times through a 5-dimensional hit-or-miss sampling procedure
891 to generate the MC events. This produces MC P_x, P_y, P_z, X, Y distributions with the
892 same momentum and position distributions as data, with the additional benefit of
893 accounting for the correlations between the considered variables. As an example, the
894 results of the DDMC generation compared to data for the kaon +100A sample are
895 shown in figure 2.5 for the P_z , X and Y distributions; as expected, MC and data agree
896 within the statistical uncertainty by construction. A LArSoft simulation module then
897 launches single particle MC from $z = -100$ cm (the location of the WC4) using the
898 MC generated events. The particles are free to decay and interact in their path from
899 WC4 to the TPC according to the Geant4 simulation.

900 Using the DDMC technique ensures that the MC and data particles have very

901 similar momentum, position and angular distributions at WC4 and allows us to use
 902 the MC sample in several occasions, for example to calibrate the energy loss upstream
 903 of the TPC (see Section 2.2.3) or to study the tracking and the calorimetric perfor-
 904 mance (sections 2.3 and 2.4). A small caveat is in order here: the DDMC is a single
 905 particle Monte Carlo, which means that the beam pile-up is not simulated.

906 Six samples are the basis fo the MC used in the pion cross section measurement:
 907 three samples of ~ 340000 pions, muons and electrons to simulate the negative 60A
 908 runs, and three samples of ~ 340000 pions, muons and electrons for the negative 100A
 909 runs.

910 The MC used for the kaon cross section analysis is a sample of **NUMBERS** kaons.

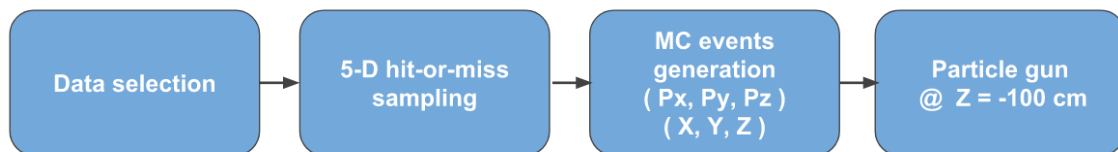


Figure 2.3: Workflow for Data Driven single particle Monte Carlo production.

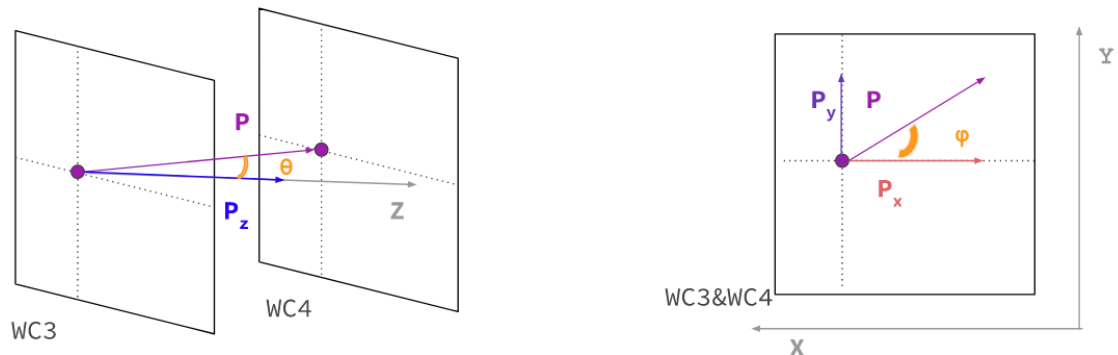


Figure 2.4: Scheme of the quantities of interest for the DDMC event generation: P_x, P_y, P_z, X, Y at WC4.

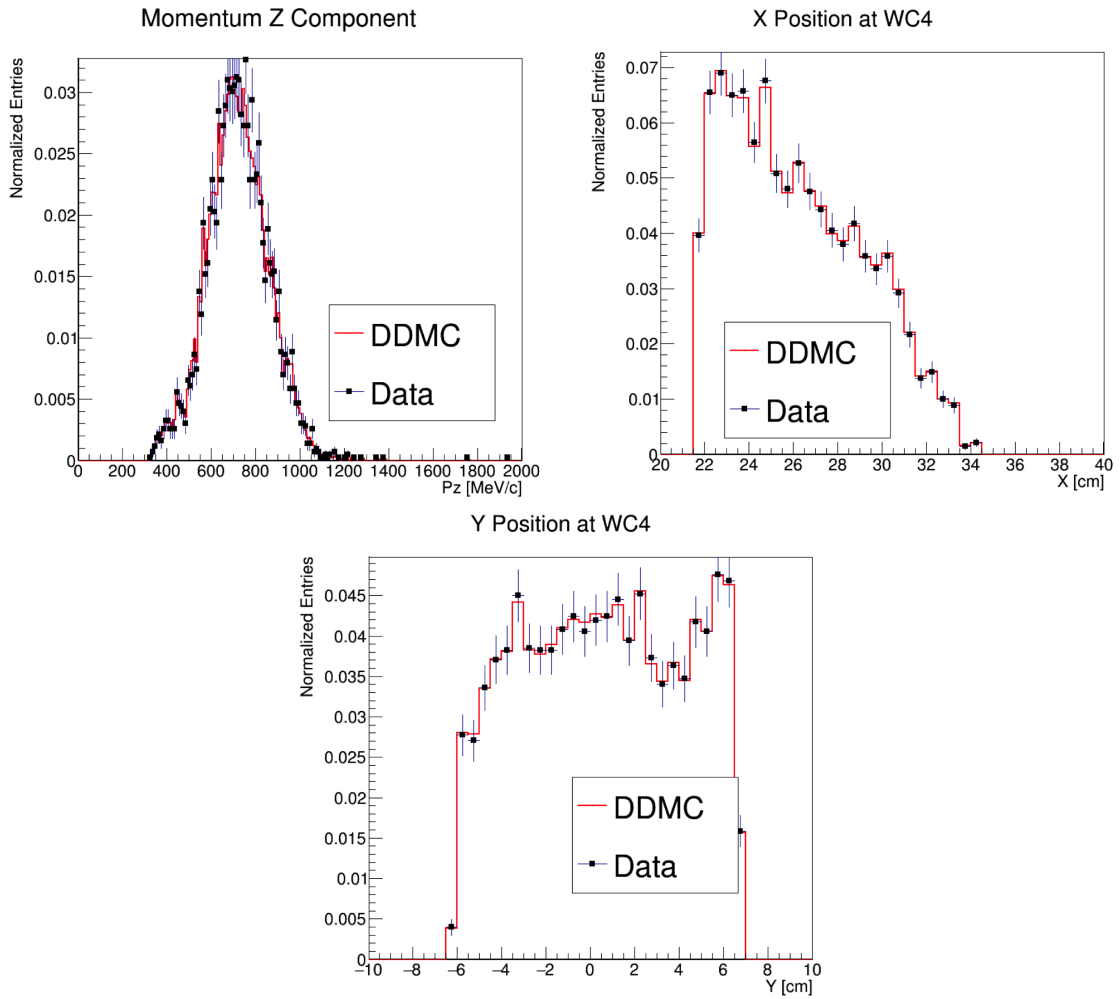


Figure 2.5: Comparison between generated quantities and data distributions for the 100A kaon sample: Z component of the momentum at WC4 (top left), X position at Wire Chamber 4 (top right), Y position at Wire Chamber 4 (bottom).

911 2.2.3 Estimate of Energy Loss before the TPC

912 The beamline particles travel a path from where their momentum is measured in
 913 the beamline until they are tracked again inside the TPC. In the LArIAT geometry,
 914 a particle leaving the WC4 will encounter the materials listed in Table 2.3 before
 915 being registered again. The energy lost by the particle in this non-instrumented
 916 material modifies the particle’s kinetic energy and directly affects the cross section
 917 measurement, as shown in equation 1.5.

Material	density [g/cm ³]	width [cm]
Fiberglass laminate (G10)	1.7	1.28
Liquid Argon	1.4	3.20
Stainless Steel	7.7	0.23
Titanium	4.5	0.04
Air	$1.2 \cdot 10^{-3}$	89.43
Plastic Scintillator	1.03	1.20 (+ 1.30)

Table 2.3: LArIAT material budget from WC4 to the TPC Front Face.

We derive an estimate of the energy loss between the beamline momentum measurement and the TPC (E_{loss}) from the pion DDMC sample, since this quantity is not measurable directly on data. The E_{loss} distribution for the 60A and 100A pion sample is shown in figure 2.6, left and right respectively. A clear double peaked structure is visible, which is due to the particles either missing or hitting the HALO paddle: a schematic rendering of this occurrence is shown in figure 2.7. The kinematic at WC4 determines the trajectory of a particle and whether or not it will hit the halo paddle. In figure 2.8 , we plot the true horizontal component of the momentum P_x versus the true X position at WC4 for pions missing the halo paddle (left) and for pions hitting the halo paddle (right) for the 60A MC simulation runs – analogous plots are obtained with the 100A simulation. These distributions can be separated drawing a line in this position-momentum space. We use a logistic regression [8] as a classifier to find the best separating line, shown in both plots as the red line. We classify as

“hitting the halo paddle” all pions whose P_x and X are such that

$$P_x + 0.02 * X - 0.4 < 0$$

and as “missing the halo paddle” all pions whose P_x and X are such that

$$P_x + 0.02 * X - 0.4 > 0,$$

where the coefficients of the line are empirically found by the logistic regression estimation. Overall, this simple method classifies in the right category (hit or miss) about 86% of the pion events. In MC, we assign $E_{loss} = 32 \pm 4$ MeV for pion events classified as “hitting the halo paddle”; we assign $E_{loss} = 24 \pm 3$ MeV for pion events classified as “missing the halo paddle”. We apply the same classifier on data. A scan of the simulated geometry showed an excess of 3 cm of un-instrumented argon compared with the surveyed detector geometry. We account for this difference by assigning in data $E_{loss} = 24 \pm 6$ MeV for pion events classified as “hitting the halo paddle” and $E_{loss} = 17 \pm 6$ MeV for pion events classified as “missing the halo paddle”, where the uncertainty is derived as the standard deviation of the double peaked distribution.

The summary of the values for used for E_{Loss} for the pion sample is listed in table 2.4 with the analogous results for the study on the kaon case.

	E_{loss} [MeV]	
	Hitting Halo	Missing Halo
Pion MC	32 ± 4	24 ± 3
Pion Data	25 ± 6	17 ± 6
Kaon MC	37 ± 5	31 ± 4
Kaon Data	26 ± 6	22 ± 6

Table 2.4: Energy loss for pions and kaons.

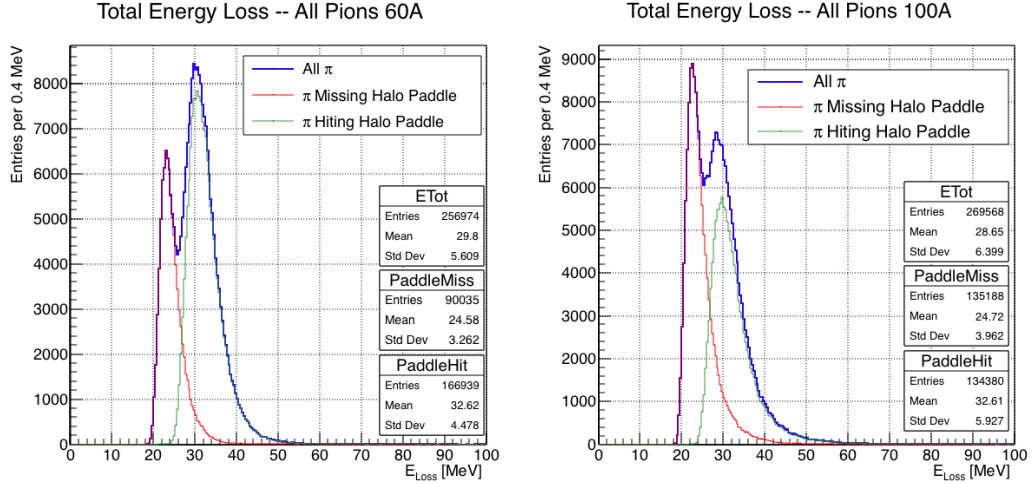


Figure 2.6: True energy loss between WC4 and the TPC front face according to the MC simulation of negative pions of the 60A runs (left) and of the 100A runs (right). The distribution for the whole data sample is shown in blue, the distribution for the pions missing the halo is shown in red, and the distribution for the pions hitting the halo is shown in green.

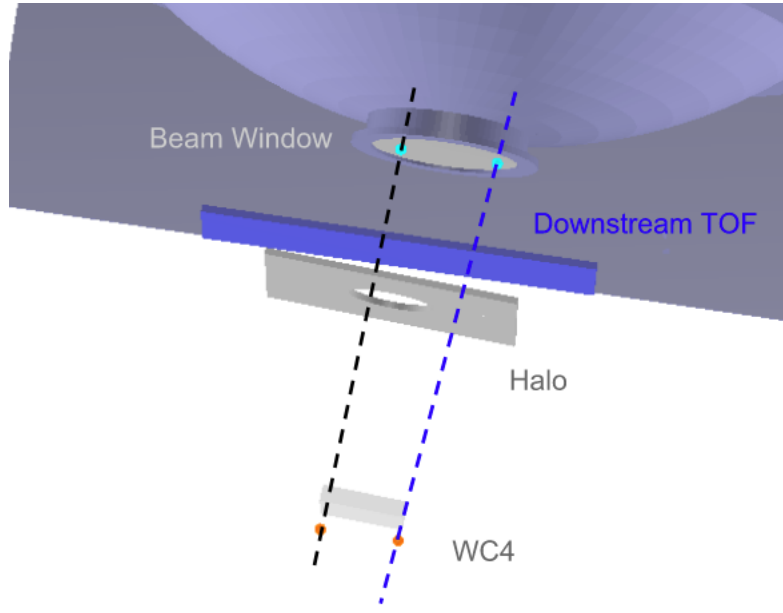


Figure 2.7: Schematic rendering of the particle path between WC4 and the TPC front face. The paddle with the hollow central circle represents the Halo paddle. We illustrate two possible trajectories: in black, a trajectory that miss the paddle and goes through the hole in the Halo, in blue a trajectory that hits the Halo paddle and goes through the scintillation material.

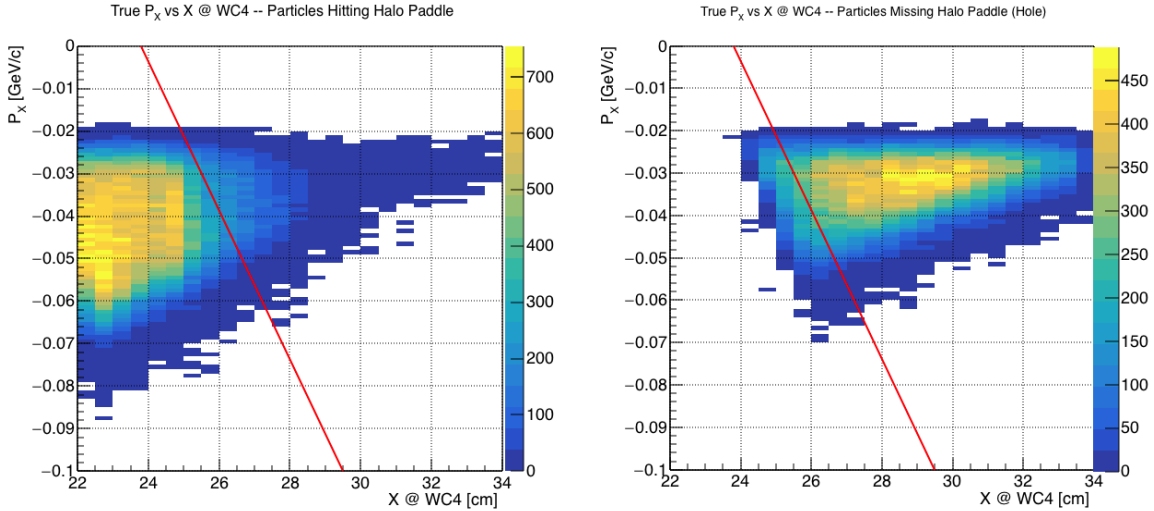


Figure 2.8: Horizontal component of the true momentum vs the horizontal position at WC4 for MC simulated pions of the 60A runs. The plot on the left shows the distribution for pion that miss the halo paddle and the plot on the right shows the distributions for pions that hit the halo. The form of the classifier is overlaid to both plots (red line).

931 2.3 Tracking Studies

932 In this section, we describe three studies. The first is a justification of the selection
 933 criteria for the beamline handshake with the TPC information. We perform this
 934 study to boost the correct identification of the particles in the TPC associated with
 935 the beamline information, while maintaining sufficient statistics for the cross section
 936 measurement. The second study is an optimization of the tracking algorithm, with
 937 the scope of maximizing the identification of the hadronic interaction point inside the
 938 TPC. These two studies are related, since the optimization of the tracking is per-
 939 formed on TPC tracks which have been matched to the wire chamber track; in turn,
 940 the tracking algorithm for TPC tracks determines the number of reconstructed tracks
 941 in each event used to try the matching with the wire chamber track. Starting with
 942 a sensible tracking reconstruction, we perform the WC2TPC matching optimization
 943 first, then the tracking optimization. The WC2TPC match purity and efficiency are
 944 then calculated again with the optimized tracking.

945 The third study is an evaluation of the angular resolution of the tracking algorithm
946 in data and MC, which is particularly important in the context of the cross section
947 analyses.

948 **2.3.1 Study of WC to TPC Match**

949 Plots I want in this section:

- 950 1. WC2TPC MC DeltaX, DeltaY and α

951 Scope of this study is assessing the goodness of the wire chamber to TPC match
952 on Monte Carlo and decide the selection values we will use on data. A word of caution
953 is necessary here. With this study, we want to minimize pathologies associated with
954 the presence of the primary hadron itself, e.g. the incorrect association between the
955 beamline hadron and its decay products inside the TPC. Assessing the contamination
956 from pile-up¹, albeit related, is beyond the scope of this study.

957 In MC, we are able to define a correct WC2TPC match using the Geant4 truth
958 information. We are thus able to count how many times the WC tracks is associated
959 with the wrong TPC reconstructed track.

960 We define a correct match if the all following conditions are met:

- 961 - the length of the true primary Geant4 track in the TPC is greater than 2 cm,
962 - the length of the reconstructed track length is greater than 2 cm,
963 - the Z position of the first reconstructed point is within 2 cm from the TPC
964 front face
965 - the distance between the reconstructed track and the true entering point is the
966 minimum compared with all the other reconstructed tracks.

1. We remind the reader that the DDMC is a single particle Monte Carlo, where the beam pile up is not simulated.

967 In order to count the wrong matches, we consider all the reconstructed tracks
 968 whose Z position of the first reconstructed point lies within 2 cm from the TPC front
 969 face. Events with true length in TPC < 2 cm are included. Since hadrons are shot
 970 100 cm upstream from the TPC front face, the following two scenarios are possible
 971 from a truth standpoint:

972 [Ta] the primary hadron decays or interact strongly before getting to the TPC,

973 [Tb] the primary hadron enters the TPC.

974 As described in Section 1.2, we define a WC2TPC match according to the relative
 975 position of the WC and TPC track parametrized with ΔR and the angle between
 976 them, parametrized with α . Once we choose the selection values r_T and α_T to de-
 977 termine a reconstructed WC2TPC match, the following five scenarios are possible in
 978 the truth to reconstruction interplay :

979 1) only the correct track is matched

980 2) only one wrong track is matched

981 3) the correct track and one (or more) wrong tracks are matched

982 4) multiple wrong tracks matched.

983 5) no reconstructed tracks are matched

984 Since we keep only events with one and only one match, we discard cases 3), 4)
 985 and 5) from the events used in the cross section measurement. For each set of r_T and
 986 α_T selection value, we define purity and efficiency of the selection as follows:

$$\text{Efficiency} = \frac{\text{Number of events correctly matched}}{\text{Number of events with primary in TPC}}, \quad (2.1)$$

$$\text{Purity} = \frac{\text{Number of events correctly matched}}{\text{Total number of matched events}}. \quad (2.2)$$

987 Figure 2.9 shows the efficiency (left) and purity (right) for WC2TPC match as a
 988 function of the radius, r_T , and angle, α_T , selection value. It is apparent how both
 989 efficiency and purity are fairly flat as a function of the radius selection value at a
 990 given angle. This is not surprising. Since we are studying a single particle gun Monte
 991 Carlo sample, the wrong matches can occur only for mis-tracking of the primary or
 992 for association with decay products; decay products will tend to be produced at large
 993 angles compared to the primary, but could be fairly close to the in x and y projection
 994 of the primary. The radius cut would play a key role in removing pile up events.

995 For LArIAT cross section measurements, we generally prefer purity over efficiency,
 996 since a sample of particles of a pure species will lead to a better measurement. Ob-
 997 viously, purity should be balanced with a sensible efficiency to avoid rejecting the
 998 whole sample.

999 We choose $(\alpha_T, r_T) = (8 \text{ deg}, 4 \text{ cm})$ and get a MC 85% efficiency and 98% purity
 1000 for the kaon sample and a MC 95% efficiency and 90% purity for the pion sample.

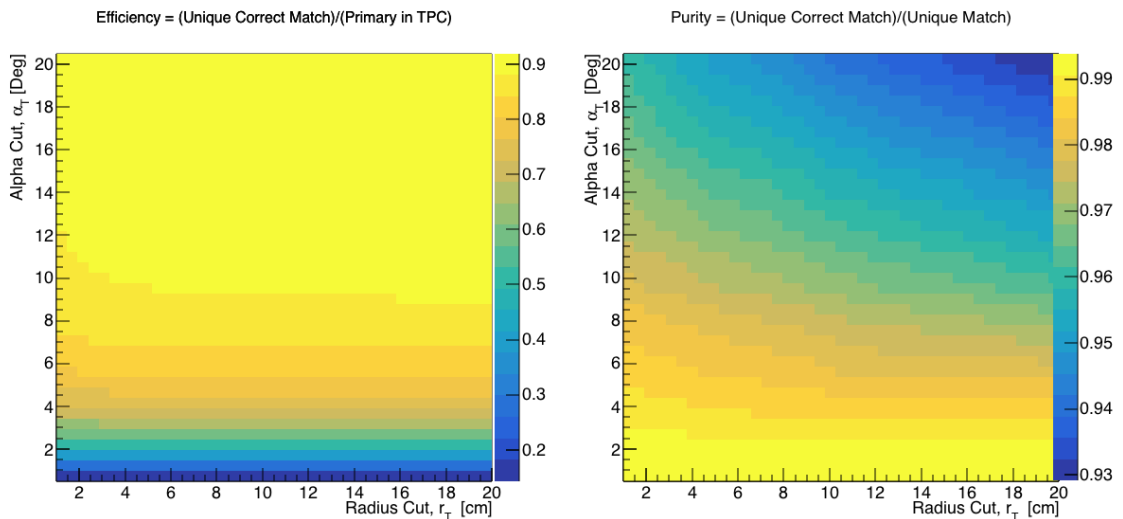


Figure 2.9: Efficiency (left) and purity (right) for WC2TPC match as a function of the radius and angle selections for the kaon sample.

1001 **2.3.2 Tracking Optimization**

1002 **2.3.3 Angular Resolution**

1003 Scope of this study is to understand and compare the tracking performances and
1004 angular resolution of the TPC tracking on data and MC. We use the angular resolution
1005 of the tracking to determine the value of smallest angle that we can reconstruct with
1006 a non-zero efficiency, effectively determining a selection on the angular distribution
1007 of the cross section measurement due to the tracking performance. This study is
1008 performed on the pion sample, but its results are extrapolated to the kaon case.

1009 We start by selecting all the WC2TPC matched tracks used for the cross section
1010 analysis. These tracks can contain from a minimum of 3 3D-space points to a maxi-
1011 mum of 240 3D-space points. We fit a line to all the 3D-space points associated with
1012 the track. For each track we calculate the average distance between each point in
1013 space and the fit line as follows

$$\bar{d} = \frac{\sum_i^N d_i}{N}, \quad (2.3)$$

1014 where N is the number of 3D-space points of the track and d_i is the distance of the
1015 i -th space point to the line fit. Several tests to compare the goodness of fit between
1016 data and MC have been considered. We decided to use \bar{d} for its straightforward
1017 interpretation. The \bar{d} distribution for data and MC is shown in Figure 2.10 and
1018 shows a relatively good agreement between data and MC.

1019 A visual representation of the procedure used to evaluate the angular resolution is
1020 shown in Figure 2.12. For each track, we order the space points according to their Z
1021 position along the positive beam direction (panel a) and we split them in two sets: the
1022 first set contains all the points belonging to the first half of the track and the second
1023 set contains all the points belonging the second half of the track. We remove the last
1024 four points in the first set and the first four points in the second set, so to have a
1025 gap in the middle of the original track (panel b). We fit the first and the second set

1026 of points with two lines (panel c). We then calculate the angle between the fit of the
 1027 first and second half α (panel d). The angle α determines the spatial resolution of
 1028 the tracking. The distributions for data and MC for α are given in Figure 2.11. The
 1029 mean of the data and MC angular resolution are respectively

$$\bar{\alpha}_{Data} = (5.0 \pm 4.5) \text{ deg}, \quad (2.4)$$

$$\bar{\alpha}_{MC} = (4.5 \pm 3.9) \text{ deg}. \quad (2.5)$$

1030 Interaction angles smaller than the angle resolution are indistinguishable for the
 1031 reconstruction. Therefore, we assess our ability to measure the cross section to be
 1032 limited to interaction angles greater than 5.0 deg. More accurate studies of the angular
 1033 resolution as a function of the kinetic energy and track length, albeit interesting, are
 1034 left for an improvement of the analysis.

1035 It is beneficial to take a moment to describe the definition of interaction angle.
 1036 In case of elastic scattering, the definition is straightforward: the interaction angle is
 1037 the angle between the incoming and outgoing pion, i.e.

$$\theta = \cos^{-1} \left(\frac{\vec{p}_{\text{incoming}} \cdot \vec{p}_{\text{outgoing}}}{|\vec{p}_{\text{incoming}}| |\vec{p}_{\text{outgoing}}|} \right). \quad (2.6)$$

1038 In case of inelastic scattering, the presence of several topologies requires a more
 1039 complex definition, as shown in figure 2.13. We define the scattering angle as the
 1040 biggest of the angles between the incoming pion and the visible daughters, where the
 1041 visible daughters are charged particles that travel more than 0.47 cm in the detector
 1042 (see panel a); in case all the daughters are invisible, the angle is assigned to be 90
 1043 deg (see panel b). We chose this working definition of scattering angle for inelastic
 1044 scattering keeping in mind how our tracking reconstruction works: the tracking will
 1045 stop correctly in case of all the daughters are not visible in the detector and it is

1046 likely to stop correctly if multiple daughters form an interaction vertex. The only
 1047 “dangerous” case is the production of one charged daughter plus neutrals, which we
 1048 can study with this working definition of scattering angle (see panel c).

1049 We can see the effects of the angular resolution on the cross section by plotting the
 1050 true Geant4 cross section for interaction angles greater than a minimum interaction
 1051 angle. Figure 2.14 shows the true Geant4 cross section for interaction angles greater
 1052 than 0 deg (green), 4.5 deg (red), 5.0 deg (blue) and 9.0 deg (yellow). A small 0.5 deg
 1053 systematic shift between the mean of the data and MC angular resolution is present.

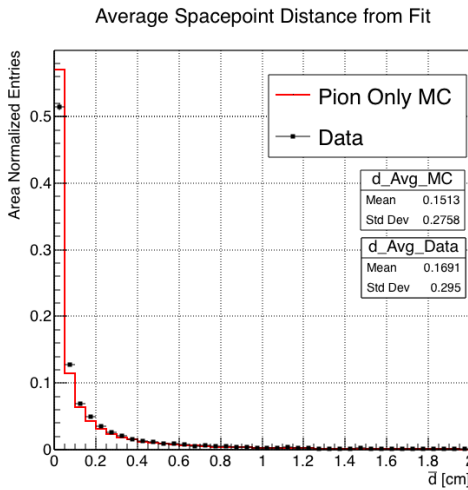


Figure 2.10: Distributions of the average distance between each 3D point in space and the fit line, \bar{d} for the data used in the pion cross section analysis and the pion only DDMC. The distributions are area normalized.

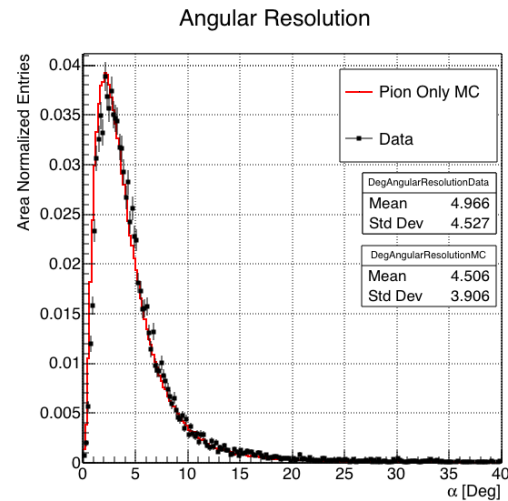


Figure 2.11: Distributions of angular resolution α for data used in the pion cross section analysis and pion only DDMC. The distributions are area normalized.

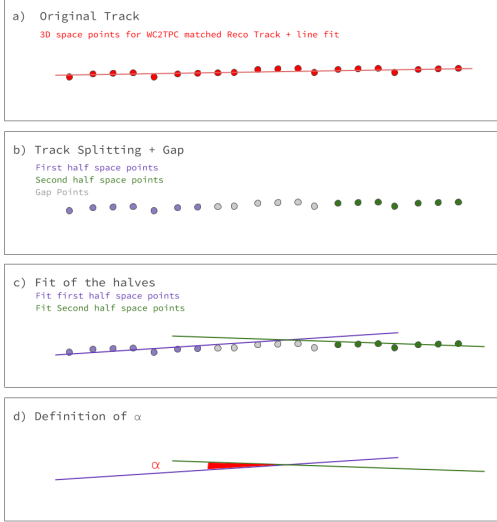


Figure 2.12: A visual representation of the procedure used to evaluate the angular resolution.

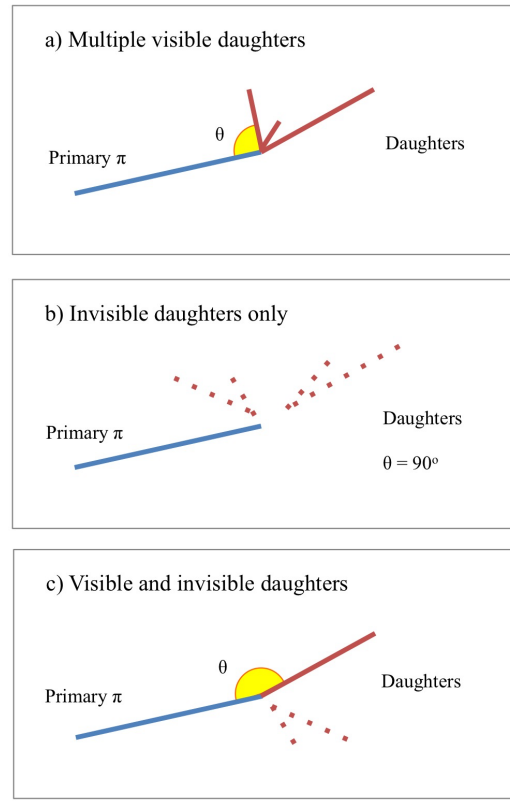


Figure 2.13: A visual representation of the scattering angle definition in case of inelastic scattering.

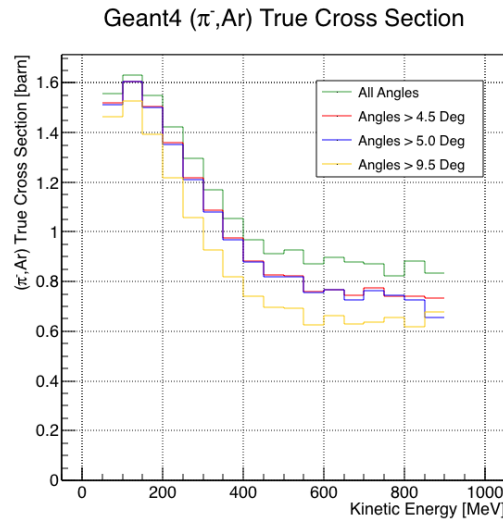


Figure 2.14: True (π^- , Ar) cross section for interaction angles greater than 0 deg (green), 4.5 deg (red), 5.0 deg (blue) and 9.0 deg (yellow).

1054 **2.4 Calorimetry Studies**

1055 The ability to measure the kinetic energy of hadrons in the TPC is fundamental
1056 for the cross section analyses. Thus, we describe first how we calibrate the TPC
1057 calorimetric response (Section 2.4.1) and how we measure the kinetic energy of the
1058 hadrons in the TPC (Section 2.4.2).

1059 **2.4.1 Energy Calibration**

1060 Scope of the energy calibration is to identify the factors which convert the charge
1061 collected (dQ) to energy deposited in the chamber (dE). As described in section
1062 0.1.5, this is a multi-step procedure. In LArIAT, we first correct the raw charge by
1063 the electronic noise on the considered wire [44], then by the electron lifetime [45],
1064 and then by the recombination using the ArgoNeut recombination values. Lastly, we
1065 apply overall calibration of the energy, i.e. we determine the “calorimetry constants”
1066 using the procedure described in this section.

1067 We independently determine the calorimetry constants for Data and Monte Carlo
1068 in the LArIAT Run-II Data samples using a parametrization of the stopping power
1069 (a.k.a. energy deposited per unit length, dE/dX) as a function of momentum. This is
1070 done by comparing the stopping power measured on reconstructed quantities against
1071 the Bethe-Bloch theoretical prediction for various particle species (see Equation 1).
1072 We obtain the theoretical expectation for the dE/dX most probable value of pions
1073 (π), muons (μ), kaons (K), and protons (p) in the momentum range most relevant
1074 for LArIAT (Figure 2.15) using the tables provided by the Particle Data Group [43]
1075 for liquid argon [1].

1076 The basic idea of this calibration technique is to utilize a sample of beamline
1077 events with known particle species and momentum to measure the dE/dX of the
1078 corresponding tracks in the TPC. In particular, we decided to use positive pions as

1079 calibration sample and samples from all the other particle species as cross check. Once
1080 the dE/dX of the positive pion sample has been measured at various momenta, we
1081 tune to calorimetry constants within the reconstruction software to align the measured
1082 values to match the theoretical ones found in Figure 2.15.

1083 In data, we start by selecting a sample of beamline positive pion beamline can-
1084 didates without any restriction on their measured momentum². We then apply the
1085 WC2TPC match and subtract the energy loss upstream to the TPC front face, de-
1086 termining the momentum at the TPC front face. For each surviving pion candidate,
1087 we measure the dE/dx at each of the first 12 spacepoints associated the 3D recon-
1088 structed track, corresponding to a ~ 5 cm portion. These dE/dX measurements are
1089 then put into a histogram that corresponds to measured momentum of the track.
1090 The dE/dX histograms are sampled every 50 MeV/c in momentum (e.g. 150 MeV/c
1091 $< P <$ 200 MeV/c, 200 MeV/c $< P <$ 250/c MeV, etc...). This process of selecting,
1092 sampling, and recording the dE/dX for various momentum bins is repeated over the
1093 entire sample of events, allowing us to collect sufficient statistic in most of the mo-
1094 mentum bins between 150 MeV/c and 1100 MeV/c. On average, pions and muons
1095 only lose ~ 10 MeV in this 5 cm section of the track and protons lose ~ 20 MeV. Thus
1096 choosing 50 MeV/c size bins for our histograms covers the energy spread within those
1097 bins due to energy loss from ionization for all the particle species identifiable in the
1098 beamline. Each 50 MeV/c momentum binned dE/dX histogram is now fit with a
1099 simple Landau function. The most probable value (MPV) and the associated error
1100 on the MPV from the fit are extracted and plotted against the theoretical prediction
1101 Figure 2.15. Depending on the outcome of the data-prediction comparison, we modify
1102 the calorimetry constants and we repeat the procedure until a qualitative agreement
1103 is achieved. We perform this tuning for the collection and induction plane separately.
1104 As a cross check to the calorimetry constants determined using the positive pions,

2. it should be noted that some muon and position contamination is present in the π^+ sample

we lock the constants and plot the dE/dx versus momentum distribution of all the other particle species identifiable in the beamline data ($\pi/\mu/e$, K , p, in both polarities) against the corresponding Beth-Bloch prediction. The agreement between data from the other particle species and the predictions is the expected result of this cross check. The results of the tuning and cross check for Run-II data on the collection plane is shown in Figure 2.16 negative polarity data on top, positive polarity data on the bottom.

In MC, we simulate the corresponding positive pion sample with the DDMC (see section 2.2.2) and follow the same steps as in data. More details on the calorimetry tuning can be found in [33].

1115 Add agreement between data and MC for dedx for pions

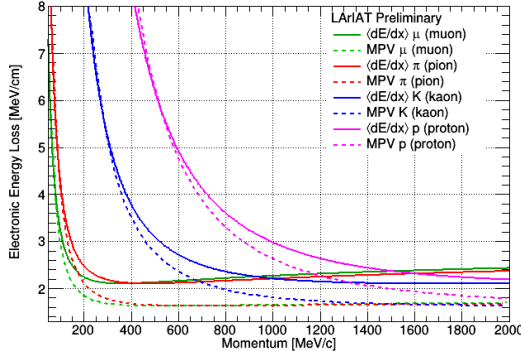


Figure 2.15: Stopping power for pions, muons, kaons, and protons in liquid argon over the momentum range most relevant for LArIAT according to the Beth-Bloch equation. The solid lines represent the prediction for the mean energy dE/dX , while the dashed lines are the predictions for the MPV.

1116 2.4.2 Kinetic Energy Measurement

The measured kinetic energy of a hadron candidate at each argon slab determines which bins of the interacting and incident histograms a selected event is going to fill. In this section, we define the measurement on the kinetic energy and determine the related uncertainty. We will propagate this uncertainty into the cross section

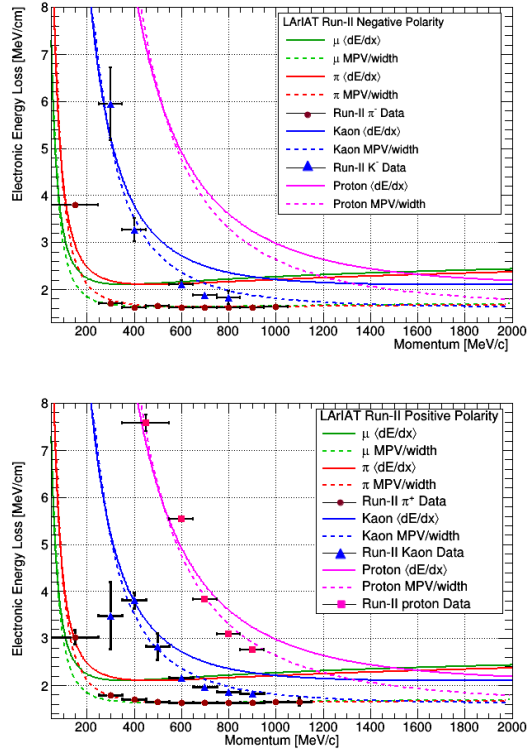


Figure 2.16: Stopping power versus Momentum for Run-II negative (top) and positive (bottom) polarity data. We achieve the agreement between the Bethe-Bloch predictions and the distribution obtained with of the positive pions (top plot, red dots) by tuning the calorimetry constants. Once the calorimetry constants are locked in, the agreement between the other particle species and the Bethe-Bloch predictions follows naturally.

measurement, as discussed in Section 3.1.2 for the pion cross section and in Section ?? for the kaon cross section.

The kinetic energy of a hadron at the j^{th} slice of argon in the TPC is given by

$$KE_j = \sqrt{p_{\text{Beam}}^2 + m_{\text{Beam}}^2} - m_{\text{Beam}}^2 - E_{\text{Loss}} - E_{\text{FF-j}}, \quad (2.7)$$

where p_{Beam} is the momentum measured by the beamline detectors, m_{Beam} is the mass of the hadron as reported in the PDG, E_{Loss} is the energy loss between the beamline and the TPC, and $E_{\text{FF-j}}$ is the energy that the hadron deposited from the

1127 TPC front face until the j^{th} slice. The uncertainty on KE_j is then given by

$$\delta KE_j = \sqrt{\delta p_{Beam}^2 + \delta E_{Loss}^2 + \delta E_{\text{dep FF-j}}^2}, \quad (2.8)$$

1128 where we have dropped the uncertainty on the mass, since it is orders of magnitude
1129 smaller than the other uncertainties. We assume the relative uncertainty on p_{Beam} to
1130 be 2%, and the uncertainty on the energy loss upstream to be 7 MeV, as calculated
1131 in Section 2.2.3. We describe the estimate of the uncertainty on $E_{\text{FF-j}}$ in the rest of
1132 this section.

1133 The energy deposited by the hadron from the TPC front face until the j^{th} slice is
1134 the sum of the measured energy deposited in each previous slabs E_i , i.e.

$$E_{\text{FF-j}} = \sum_{i < j} E_i, \quad (2.9)$$

1135 where E_i is measured in each slab as the product of the stopping power, dE/dX_i ,
1136 and the track pitch, $Pitch_i$, for that point. If we assume conservatively that the
1137 measurements of E_i are not independent from one another, the uncertainty on $E_{\text{FF-j}}$
1138 becomes

$$\delta E_{\text{FF-j}} = (j - 1)\delta E_i, \quad (2.10)$$

1139 where δE_i is the uncertainty on the energy loss in one slab of argon.

1140 The left side of Figure 2.17 shows the distribution of the energy deposited in each
1141 slab of argon, for the 60A negative pion dataset in black and for the pion only MC
1142 in blue. The analogous plot for the -100A negative pion data set is show on the right
1143 side of Figure 2.17. The distributions are fitted with a landau displayed in red for
1144 data and in teal for MC. The uncertainty on E_i is given by the width of the Landau
1145 fit to the data. A small systematic uncertainty is given by a 1.0% difference between
1146 the most probable value of the landau fits in data and MC.

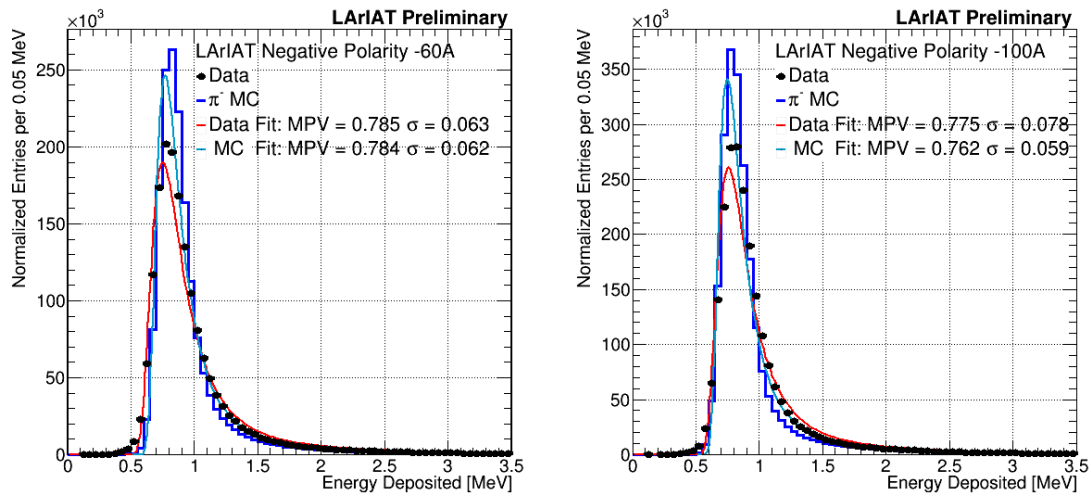


Figure 2.17: Energy deposited E_i in a single slab of argon for the pion -60A runs (left) and -100A runs (right). The data is shown in black, the MC in blue. The distributions are fitted with a landau displayed in red for data and in teal for MC.

1147 **Chapter 3**

1148 **Negative Pion Cross Section**

1149 **Measurement**

1150 **3.1 Raw Cross Section**

1151 We measure the (π^- -Ar) cross section as a function of the kinetic energy in the
1152 two chosen data sets, the 60A and 100A negative runs. As will be clarified in 3.2,
1153 the corrections to the raw cross section depend on the beam conditions and need
1154 to proceed independently for the two data sets. Thus, we present here the two
1155 measurements separately.

1156 As stated in section 1.3.2, the raw cross section is given by the equation

$$\sigma_{TOT}(E_i) = \frac{1}{n\delta X} \frac{N_{Interacting}(E_i)}{N_{Incident}(E_i)}. \quad (3.1)$$

1157 where $N_{Interacting}$ is the number of particles interacting in an argon slice at kinetic
1158 energy E_i , $N_{Incident}$ is number of particles incident on the argon slice at kinetic energy
1159 E_i , n is the density of the target centers and δX is the thickness of the argon slice.

1160 Figure 3.1 shows the interacting histogram for the 60A dataset on the left and for
1161 the 100A dataset on the right. Figure 3.2 shows the incident histogram for the 60A

dataset on the left and for the 100A dataset on the right. Figure 3.3 shows the raw cross section for the 60A dataset on the left and for the 100A dataset on the right. On all plots the same color scheme is used: the statistical uncertainty is shown in azure, while the systematic uncertainty is shown in blue. The calculation of the statistical uncertainty is laid out in section 3.1.1, while the systematics on this 3.1.2.

3.1.1 Statistical Uncertainty

The statistical uncertainty for each kinetic energy bin of the cross section plot is calculated by error propagation from the statistical uncertainty on $N_{Incident}$ and $N_{Interacting}$ correspondent bin. Since the number of incident hadrons in each energy bin is given by a simple counting, we assume that $N_{Incident}$ is distributed as a poissonian with mean and variance equal to $N_{Incident}$ in each bin. On the other hand, $N_{Interacting}$ follows a binomial distribution: a particle in a given energy bin might or might not interact. The variance for the binomial is given by

$$\text{Var}[N_{Incident}] = \mathcal{N}P_{Interacting}(1 - P_{Interacting}); \quad (3.2)$$

since the interaction probability $P_{Interacting}$ is $\frac{N_{Interacting}}{N_{Incident}}$ and the number of tries \mathcal{N} is $N_{Incident}$, equation 3.2 translates into

$$\text{Var}[N_{Incident}] = N_{Incident} \frac{N_{Interacting}}{N_{Incident}} \left(1 - \frac{N_{Interacting}}{N_{Incident}}\right) = N_{Interacting} \left(1 - \frac{N_{Interacting}}{N_{Incident}}\right). \quad (3.3)$$

$N_{Incident}$ and $N_{Interacting}$ are not independent. The statistical uncertainty on the cross section is thus calculated as

$$\delta\sigma_{tot}(E) = \sigma_{tot}(E) \left(\frac{\delta N_{Interacting}}{N_{Interacting}} + \frac{\delta N_{Incident}}{N_{Incident}} \right) \quad (3.4)$$

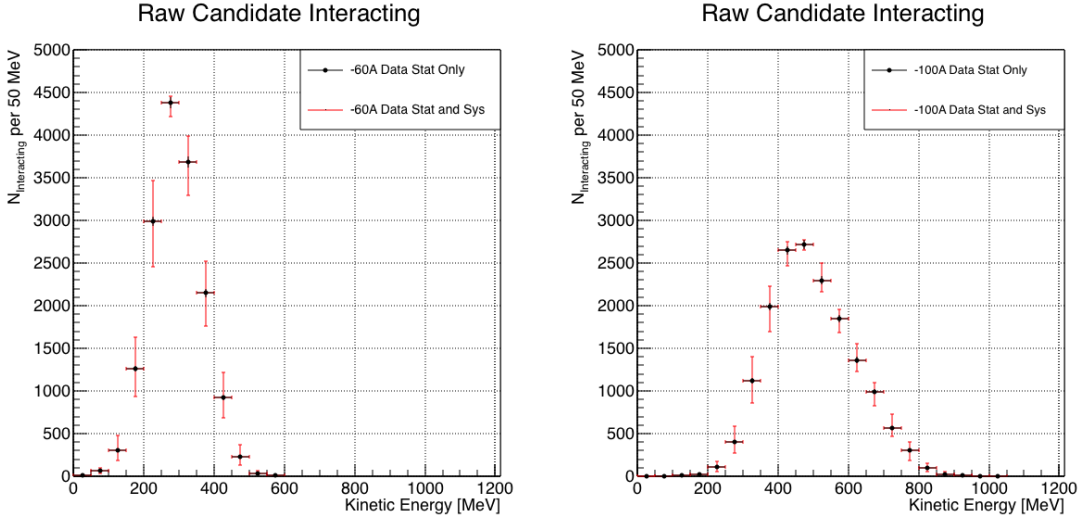


Figure 3.1: Raw number of interacting pion candidates as a function of the reconstructed kinetic energy for the 60A runs (lef) and for the 100A runs (right). The statistical uncertainties are shown in azure, the systematic uncertainties in blue.

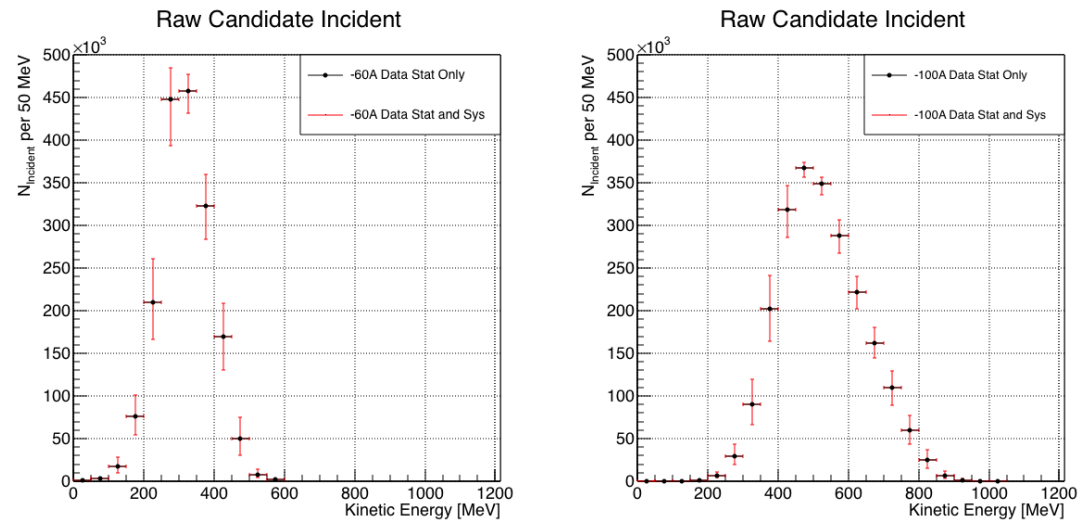


Figure 3.2: Raw number of incident pion candidates as a function of the reconstructed kinetic energy for the 60A runs (lef) and for the 100A runs (right). The statistical uncertainties are shown in azure, the systematic uncertainties in blue.

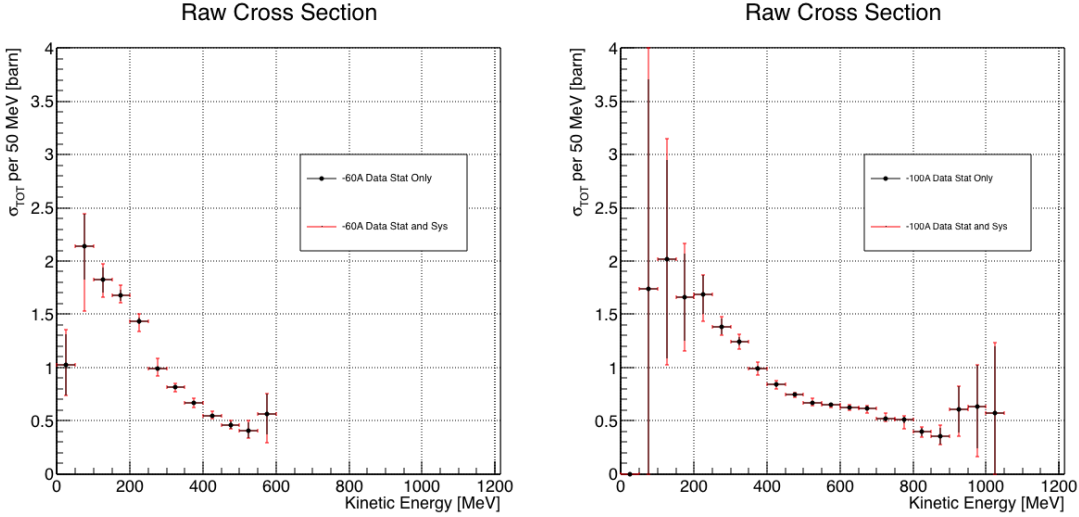


Figure 3.3: Raw (π^- -Ar) total hadronic cross section for the 60A runs (lef) and for the 100A runs (right). The statistical uncertainties are shown in azure, the systematic uncertainties in blue.

¹¹⁷⁹ where:

$$\delta N_{Incident} = \sqrt{N_{Incident}} \quad (3.5)$$

$$\delta N_{Interacting} = \sqrt{N_{Interacting} \left(1 - \frac{N_{Interacting}}{N_{Incident}}\right)}. \quad (3.6)$$

¹¹⁸⁰ 3.1.2 Treatment of Systematics

¹¹⁸¹ The only systematic effect considered in the measurement of the raw cross section
¹¹⁸² come from the propagation of the uncertainty associate with the measurement of the
¹¹⁸³ kinetic energy at each slab.

¹¹⁸⁴ 3.2 Corrections to the Raw Cross Section

¹¹⁸⁵ 3.2.1 Treatment of Systematics

₁₁₈₆

Bibliography

- ₁₁₈₇ [1] PDG Tables for Liquid Argon. . Technical report.
- ₁₁₈₈ [2] R Acciarri, C Adams, J Asaadi, B Baller, T Bolton, C Bromberg, F Ca-
₁₁₈₉ vanna, E Church, D Edmunds, A Ereditato, S Farooq, B Fleming, H Greenlee,
₁₁₉₀ G Horton-Smith, C James, E Klein, K Lang, P Laurens, D McKee, R Mehdiyev,
₁₁₉₁ B Page, O Palamara, K Partyka, G Rameika, B Rebel, M Soderberg, J Spitz,
₁₁₉₂ A M Szelc, M Weber, M Wojcik, T Yang, and G P Zeller. A study of electron
₁₁₉₃ recombination using highly ionizing particles in the argoneut liquid argon tpc.
₁₁₉₄ *Journal of Instrumentation*, 8(08):P08005, 2013.
- ₁₁₉₅ [3] R Acciarri, M Antonello, B Baibussinov, M Baldo-Ceolin, P Benetti, F Calaprice,
₁₁₉₆ E Calligarich, M Cambiaghi, N Canci, F Carbonara, F Cavanna, S Centro, A G
₁₁₉₇ Cocco, F Di Pompeo, G Fiorillo, C Galbiati, V Gallo, L Grandi, G Meng, I Mod-
₁₁₉₈ ena, C Montanari, O Palamara, L Pandola, G B Piano Mortari, F Pietropaolo,
₁₁₉₉ G L Raselli, M Roncadelli, M Rossella, C Rubbia, E Segreto, A M Szelc, S Ven-
₁₂₀₀ tura, and C Vignoli. Effects of nitrogen contamination in liquid argon. *Journal*
₁₂₀₁ *of Instrumentation*, 5(06):P06003, 2010.
- ₁₂₀₂ [4] R. Acciarri et al. Design and Construction of the MicroBooNE Detector. *JINST*,
₁₂₀₃ 12(02):P02017, 2017.
- ₁₂₀₄ [5] R. Acciarri et al. First Observation of Low Energy Electron Neutrinos in a Liquid
₁₂₀₅ Argon Time Projection Chamber. *Phys. Rev.*, D95(7):072005, 2017. [Phys.

- 1206 Rev.D95,072005(2017)].
- 1207 [6] M Adamowski, B Carls, E Dvorak, A Hahn, W Jaskierny, C Johnson, H Jostlein,
1208 C Kendziora, S Lockwitz, B Pahlka, R Plunkett, S Pordes, B Rebel, R Schmitt,
1209 M Stancari, T Tope, E Voirin, and T Yang. The liquid argon purity demonstrator.
1210 *Journal of Instrumentation*, 9(07):P07005, 2014.
- 1211 [7] C. Adams et al. The Long-Baseline Neutrino Experiment: Exploring Fundamen-
1212 tal Symmetries of the Universe. 2013.
- 1213 [8] Alan Agresti. *Categorical Data Analysis*. Wiley Series in Probability and Statis-
1214 tics. Wiley, 2013.
- 1215 [9] A. Aguilar-Arevalo et al. Evidence for neutrino oscillations from the observa-
1216 tion of anti-neutrino(electron) appearance in a anti-neutrino(muon) beam. *Phys.*
1217 *Rev.*, D64:112007, 2001.
- 1218 [10] A. A. Aguilar-Arevalo et al. Improved Search for $\bar{\nu}_\mu \rightarrow \bar{\nu}_e$ Oscillations in the
1219 MiniBooNE Experiment. *Phys. Rev. Lett.*, 110:161801, 2013.
- 1220 [11] S. Amoruso et al. Study of electron recombination in liquid argon with the
1221 ICARUS TPC. *Nucl. Instrum. Meth.*, A523:275–286, 2004.
- 1222 [12] C. Anderson et al. The ArgoNeuT Detector in the NuMI Low-Energy beam line
1223 at Fermilab. *JINST*, 7:P10019, 2012.
- 1224 [13] M. Antonello, B. Baibussinov, P. Benetti, E. Calligarich, N. Canci, S. Cen-
1225 tro, A. Cesana, K. Cieslik, D. B. Cline, A. G. Cocco, A. Dabrowska, D. De-
1226 qual, A. Dermenev, R. Dolfini, C. Farnese, A. Fava, A. Ferrari, G. Fiorillo,
1227 D. Gibin, S. Gninenko, A. Guglielmi, M. Haranczyk, J. Holeczek, A. Ivashkin,
1228 J. Kisiel, I. Kochanek, J. Lagoda, S. Mania, A. Menegolli, G. Meng, C. Monta-
1229 nari, S. Otwinowski, A. Piazzoli, P. Picchi, F. Pietropaolo, P. Plonski, A. Rap-

- 1230 poldi, G. L. Raselli, M. Rossella, C. Rubbia, P. Sala, A. Scaramelli, E. Seg-
1231 reto, F. Sergiampietri, D. Stefan, J. Stepaniak, R. Sulej, M. Szarska, M. Ter-
1232 rani, F. Varanini, S. Ventura, C. Vignoli, H. Wang, X. Yang, A. Zalewska, and
1233 K. Zaremba. Precise 3d track reconstruction algorithm for the ICARUS t600 liq-
1234 uid argon time projection chamber detector. *Advances in High Energy Physics*,
1235 2013:1–16, 2013.
- 1236 [14] M. Antonello et al. A Proposal for a Three Detector Short-Baseline Neutrino
1237 Oscillation Program in the Fermilab Booster Neutrino Beam. 2015.
- 1238 [15] C. Athanassopoulos et al. Evidence for $\nu(\mu) \rightarrow \nu(e)$ neutrino oscillations
1239 from LSND. *Phys. Rev. Lett.*, 81:1774–1777, 1998.
- 1240 [16] B. Baller. Trajcluster user guide. Technical report, apr 2016.
- 1241 [17] Gary Barker. Neutrino event reconstruction in a liquid argon TPC. *Journal of*
1242 *Physics: Conference Series*, 308:012015, jul 2011.
- 1243 [18] J B Birks. Scintillations from organic crystals: Specific fluorescence and relative
1244 response to different radiations. *Proceedings of the Physical Society. Section A*,
1245 64(10):874, 1951.
- 1246 [19] Mark G. Boulay and A. Hime. Direct WIMP detection using scintillation time
1247 discrimination in liquid argon. 2004.
- 1248 [20] W. M. Burton and B. A. Powell. Fluorescence of tetraphenyl-butadiene in the
1249 vacuum ultraviolet. *Applied Optics*, 12(1):87, jan 1973.
- 1250 [21] E. Church. LArSoft: A Software Package for Liquid Argon Time Projection Drift
1251 Chambers. 2013.
- 1252 [22] The LArIAT Collaboration. The liquid argon in a testbeam (lariat) experiment.
1253 Technical report, In Preparation 2018.

- 1254 [23] S.E. Derenzo, A.R. Kirschbaum, P.H. Eberhard, R.R. Ross, and F.T. Solmitz.
1255 Test of a liquid argon chamber with 20 m rms resolution. *Nuclear Instruments*
1256 and Methods, 122:319 – 327, 1974.
- 1257 [24] A Ereditato, C C Hsu, S Janos, I Kreslo, M Messina, C Rudolf von Rohr, B Rossi,
1258 T Strauss, M S Weber, and M Zeller. Design and operation of argontube: a 5 m
1259 long drift liquid argon tpc. *Journal of Instrumentation*, 8(07):P07002, 2013.
- 1260 [25] R. Acciarri et al. Convolutional neural networks applied to neutrino events
1261 in a liquid argon time projection chamber. *Journal of Instrumentation*,
1262 12(03):P03011, 2017.
- 1263 [26] R. Acciarri et al. Design and construction of the MicroBooNE detector. *Journal*
1264 of *Instrumentation*, 12(02):P02017–P02017, feb 2017.
- 1265 [27] C. E. Aalseth et al.l. DarkSide-20k: A 20 tonne two-phase LAr TPC for direct
1266 dark matter detection at LNGS. *The European Physical Journal Plus*, 133(3),
1267 mar 2018.
- 1268 [28] V.M. Gehman, S.R. Seibert, K. Rielage, A. Hime, Y. Sun, D.-M. Mei, J. Maassen,
1269 and D. Moore. Fluorescence efficiency and visible re-emission spectrum of
1270 tetraphenyl butadiene films at extreme ultraviolet wavelengths. *Nuclear Instru-*
1271 *ments and Methods in Physics Research Section A: Accelerators, Spectrometers,*
1272 *Detectors and Associated Equipment*, 654(1):116 – 121, 2011.
- 1273 [29] H. Geiger and E. Marsden. On a diffuse reflection of the formula-particles. *Pro-*
1274 *ceedings of the Royal Society A: Mathematical, Physical and Engineering Sci-*
1275 *ences*, 82(557):495–500, jul 1909.
- 1276 [30] C. Green, J. Kowalkowski, M. Paterno, M. Fischler, L. Garren, and Q. Lu. The
1277 Art Framework. *J. Phys. Conf. Ser.*, 396:022020, 2012.

- 1278 [31] H J Hilke. Time projection chambers. *Reports on Progress in Physics*,
1279 73(11):116201, 2010.
- 1280 [32] N. Ishida, M. Chen, T. Doke, K. Hasuike, A. Hitachi, M. Gaudreau, M. Kase,
1281 Y. Kawada, J. Kikuchi, T. Komiya, K. Kuwahara, K. Masuda, H. Okada, Y.H.
1282 Qu, M. Suzuki, and T. Takahashi. Attenuation length measurements of scintil-
1283 lation light in liquid rare gases and their mixtures using an improved reflection
1284 suppresser. *Nuclear Instruments and Methods in Physics Research Section A:*
1285 *Accelerators, Spectrometers, Detectors and Associated Equipment*, 384(2-3):380–
1286 386, jan 1997.
- 1287 [33] G. Pulliam J. Asaadi, E. Gramellini. Determination of the electron lifetime in
1288 lariat. Technical report, August 2017.
- 1289 [34] George Jaffé. Zur theorie der ionisation in kolonnen. *Annalen der Physik*,
1290 347(12):303–344, 1913.
- 1291 [35] B J P Jones, C S Chiu, J M Conrad, C M Ignarra, T Katori, and M Toups.
1292 A measurement of the absorption of liquid argon scintillation light by dissolved
1293 nitrogen at the part-per-million level. *Journal of Instrumentation*, 8(07):P07011,
1294 2013.
- 1295 [36] Benjamin J. P. Jones. *Sterile Neutrinos in Cold Climates*. PhD thesis, MIT,
1296 2015.
- 1297 [37] M A Leigui de Oliveira. Expression of Interest for a Full-Scale Detector Engi-
1298 neering Test and Test Beam Calibration of a Single-Phase LAr TPC. Technical
1299 Report CERN-SPSC-2014-027. SPSC-EOI-011, CERN, Geneva, Oct 2014.
- 1300 [38] W. H. Lippincott, K. J. Coakley, D. Gastler, A. Hime, E. Kearns, D. N. McK-
1301 insey, J. A. Nikkel, and L. C. Stonehill. Scintillation time dependence and pulse
1302 shape discrimination in liquid argon. *Phys. Rev. C*, 78:035801, Sep 2008.

- 1303 [39] M. Mooney. The microboone experiment and the impact of space charge effects.
1304 2015.
- 1305 [40] E. Morikawa, R. Reininger, P. Gürtler, V. Saile, and P. Laporte. Argon, krypton,
1306 and xenon excimer luminescence: From the dilute gas to the condensed phase.
1307 *The Journal of Chemical Physics*, 91(3):1469–1477, aug 1989.
- 1308 [41] D. R. Nygren. The time projection chamber: A new 4π detector for charged
1309 particles. Technical report, 1974.
- 1310 [42] L. Onsager. Initial recombination of ions. *Phys. Rev.*, 54:554–557, Oct 1938.
- 1311 [43] C. Patrignani et al. Review of Particle Physics. *Chin. Phys.*, C40(10):100001,
1312 2016.
- 1313 [44] T. Yang R. Acciarri. Investigation of the non-uniformity observed in the wire
1314 response to charge in lariat run 1. Technical report, February 2017.
- 1315 [45] T. Yang R. Acciarri, M. Stancari. Determination of the electron lifetime in lariat.
1316 Technical report, March 2016.
- 1317 [46] C. Rubbia. The Liquid Argon Time Projection Chamber: A New Concept for
1318 Neutrino Detectors. 1977.
- 1319 [47] R. K. Teague and C. J. Pings. Refractive index and the lorentz–lorenz function
1320 for gaseous and liquid argon, including a study of the coexistence curve near the
1321 critical state. *The Journal of Chemical Physics*, 48(11):4973–4984, jun 1968.
- 1322 [48] J. Thomas and D. A. Imel. Recombination of electron-ion pairs in liquid argon
1323 and liquid xenon. *Phys. Rev. A*, 36:614–616, Jul 1987.
- 1324 [49] N Yahlali, L M P Fernandes, K Gonzlez, A N C Garcia, and A Soriano. Imaging
1325 with sipms in noble-gas detectors. *Journal of Instrumentation*, 8(01):C01003,
1326 2013.